AD-A181 901 A NEW PUMPJET DESIGN THEORY(U) TETRA TECH INC PASADENA 1/1
CA O FURUYA ET AL 01 MAR 86 TETRAT-TC-3037
N00014-85-C-0050

UNCLASSIFIED F/G 21/5 NL

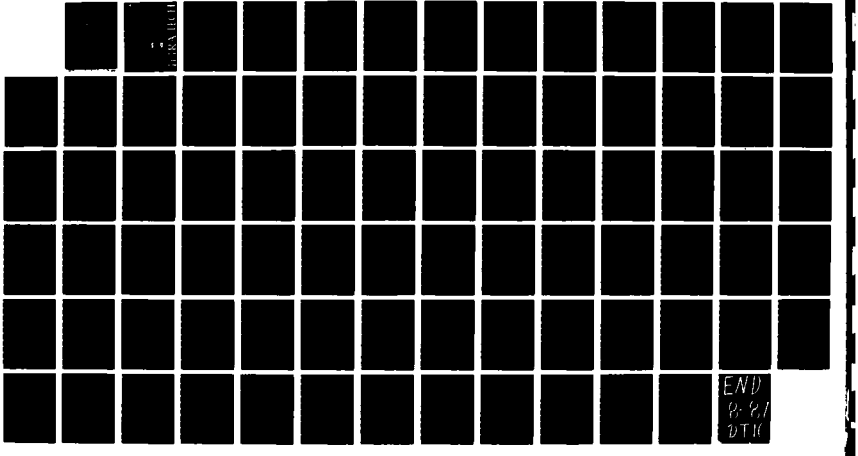

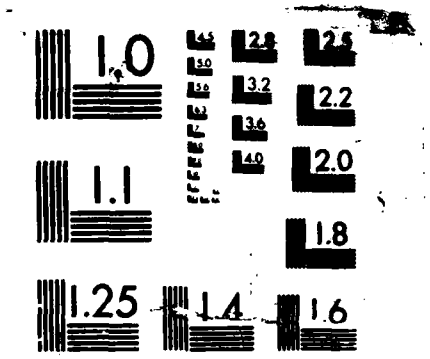

MICROCOPY RESOLUTION TEST CHART

Report No. TC-3037
Contract No. N00014-85-C-0050

(1)

A NEW PUMPJET DESIGN THEORY

by

OKITSUGU FURUYA
WEN-LI CHIANG

TETRA TECH, INC.
630 NORTH ROSEMEAD BOULEVARD
PASADENA, CALIFORNIA 91107

MARCH 1986

Prepared for

DAVID W. TAYLOR NAVAL SHIP
RESEARCH AND DEVELOPMENT CENTER
BETHESDA, MARYLAND 20084

OFFICE OF NAVAL RESEARCH
800 NORTH QUINCY STREET
ARLINGTON, VIRGINIA 22217-5000

TETRA TECH

Report No. TC-3037
Contract No. N00014-85-C-0050

A NEW PUMPJET DESIGN THEORY

by

OKITSUGU FURUYA
WEN-LI CHIANG

TETRA TECH, INC.
630 NORTH ROSEMEAD BOULEVARD
PASADENA, CALIFORNIA 91107

MARCH 1986

Prepared for

DAVID W. TAYLOR NAVAL SHIP
RESEARCH AND DEVELOPMENT CENTER
BETHESDA, MARYLAND 20084

OFFICE OF NAVAL RESEARCH
800 NORTH QUINCY STREET
ARLINGTON, VIRGINIA 22217-5000

Approved for public release;
distribution unlimited

UNCLASSIFIED

SECURITY CLASSIFICATION OF THIS PAGE (When Data Entered)

REPORT DOCUMENTATION PAGE		READ INSTRUCTIONS BEFORE COMPLETING FORM
1. REPORT NUMBER TC-3037	2. GOVT ACCESSION NO.	3. RECIPIENT'S CATALOG NUMBER
4. TITLE (and Subtitle) A NEW PUMPJET DESIGN THEORY		5. TYPE OF REPORT & PERIOD COVERED Technical - Theory & Experiment January 1, 1985 - Dec. 31, 1985 6. PERFORMING ORG. REPORT NUMBER TC-3037
7. AUTHOR(s) O. Furuya W.-L. Chiang		8. CONTRACT OR GRANT NUMBER(s) N00014-85-C-0050
9. PERFORMING ORGANIZATION NAME AND ADDRESS Tetra Tech, Inc. 630 N. Rosemead Blvd. Pasadena, CA 91107		10. PROGRAM ELEMENT, PROJECT, TASK AREA & WORK UNIT NUMBERS
11. CONTROLLING OFFICE NAME AND ADDRESS DWTNSRDC Dept. of the Navy Bethesda, MD 20084		12. REPORT DATE March 1, 1986 13. NUMBER OF PAGES 76
14. MONITORING AGENCY NAME & ADDRESS(if different from Controlling Office) Office of Naval Research 800 North Quincy St. Arlington, VA 22217-5000		15. SECURITY CLASS. (of this report) Unclassified 15a. DECLASSIFICATION/DOWNGRADING SCHEDULE

16. DISTRIBUTION STATEMENT (of this Report)

Approved for public release; distribution unlimited

17. DISTRIBUTION STATEMENT (of the abstract entered in Block 20, if different from Report)

18. SUPPLEMENTARY NOTES

Sponsored by the Naval Sea Systems Command General Hydrodynamic Research Program and administered by the David W. Taylor Naval Ship R&D Center, Code 1505, Bethesda, MD 20084.

19. KEY WORDS (Continue on reverse side if necessary and identify by block number)

Pumpjet
Streamline Curvature Method
Blade-through Flow
Blade-to-Blade Method

20. ABSTRACT (Continue on reverse side if necessary and identify by block number)

The pumpjet is a unique fluid machine which utilizes retarded wake flow and produces high propulsive efficiency such as 90%. The existing pumpjet design method is based on a simple two-dimensional graphic method which was used for pump design. As the demand for the speed of underwater vehicles increased in recent years, the existing design method became inappropriate. Effort has been made to develop a new three-dimensional pump design method by combining a blade-through flow theory with blade-to-blade flow theory. Such a method requires

DD FORM 1 JAN 73 1473 EDITION OF 1 NOV 65 IS OBSOLETE
S/N 0102-014-6601

UNCLASSIFIED

SECURITY CLASSIFICATION OF THIS PAGE (When Data Entered)

20. many supporting sub-theories to be developed. The foundation work for the blade-through flow theory, i.e., streamline curvature method, three-dimensional flow mapping technique, as well as two-dimensional cascade theory has been established in this FY-85 GHR program. Future work for completing sub-theories and incorporating such theories into a unified design theory will follow.

TABLE OF CONTENTS

LIST OF FIGURES

List of Figures (Continued)

1.0 BACKGROUND

The pumpjet is considered to be one of the most promising candidate propulsors for high speed underwater vehicles and, as a matter of fact, it has recently been employed for MK-48 torpedoes, ALWT--Advanced Light Weight Torpedo, now called MK-50 and other underwater vehicles. The pumpjet superiority over other propulsion devices is represented by two major factors, i.e., high efficiency and quietness.

The pumpjet is one of few fluid devices which positively utilizes retarded wake flow and produces high propulsive efficiency. This peculiar situation may be understood readily by considering the momentum equatin applied to a control volume surrounding an underwater vehicle, fixed to the inertial coordinate system. In the conventional propeller, for example, the velocity of flow comng into a propeller blade is approximately equal to the vehicle speed since the propeller diameter is large enough to enjoy the free stream flow. In order for the propeller to generate any effective thrust, it should accelerate the flow, the ejected flow speed being faster than the incoming flow. If one observes this situation from the inertial frame, the ejected flow has a finite positive flow speed against the surrounding environment. It means that a certain amount of the energy imparted on the fluid by the thruster is dumped in the surrounding water. On the other hand, the pumpjet receives the retarded flow velocity, slower than the free stream velocity. In order to generate a thrust, again this flow should be accelerated. However, if the pumpjet is properly designed, the accelerated flow velocity can nearly be that of the vehicle speed. If one looks at a similar control volume, from the inertial frame, the ejected flow out of the pumpjet has almost no absolute velocity and thus leaves hardly any jet wake after the vehicle passed. There exists much less wasted energy in the flow field after a vehicle with a pumpjet passes. This is the major reason why

the pumpjet can produce such high propulsive efficiency such as 90% or higher if it is properly designed.

Quietness is a guaranteed aspect with the pumpjet, as can be seen from its configuration (see Figure 1-1); a long shroud completely surrounding the rotor helps prevent rotor noise from emitting into the outside flow field. Furthermore, this "internal" flow machine has better resistance characteristics against cavitation, resulting in quieter shallow water operation where propulsors are most susceptible to cavitation.

However, in order to achieve such a high standard of performance there are many penalties to be paid in reality. The first such penalty naturally stems from the pumpjet's utilizing the velocity-retarded wake flow. A typical meridional flow distribution at the inlet of pumpjet rotor is shown in Figure 1-2; the velocity at the hub is only 30% of the free stream velocity and rapidly increases to 75% at the shroud internal boundary. This large velocity gradient in the transverse direction is, of course, built up by the viscous boundary layer effect and is one of the key features causing difficulties in design, fabrication and eventually in achieving the pumpjet high performance.

When one designs an axial or a near axial pump, it is customary to distribute the blade loading from hub to tip in a forced vortex or a free vortex distribution method, such as shown in Figure 1-3. Such distribution methods are important in obtaining as uniform a discharge jet behind the rotor as possible to minimize the mixing loss. However, a serious problem arises in attempting to implement either forced vortex or free vortex loading distribution against the flow field having a large velocity gradient, as shown in Figure 1-2. Due to the lack of enough meridional flow velocity near the hub, the blade there should be designed to have extremely large incidence angle as well as large

camber. It is for this reason that the pumpjet rotor designed to date has a distorted profile shape from hub to tip, see Figure 1-4. If this were a conventional propeller, the stagger angle would become smaller towards the hub and the camber would stay more or less constant. However, for the reason mentioned above, the pumpjet blade stagger angle first becomes smaller up to the midspan area but becomes larger toward the hub and thus the camber is designed to be substantially larger.

This unusual rotor blade setup causes various hydrodynamic problems. First of all, since a typical flow incidence angle near the hub should be surprisingly high (e.g., 30°), even a slight error in design may cause flow separation, possibly cavitation and then noise generation. Secondly, even if design is made properly, the same vulnerable situation is generated with a slight flow disturbance or blade deformation due to fabrication inaccuracy.* A recent study at Tetra Tech (see the report by Furuya, et al. (1984)) indicated that some blade deformation, particularly near the hub, could cause an increase of the power coefficient, C_p, by as much as 7.3% (see Figure 1-5). Furthermore, there exists a profound discrepancy between water tunnel test results and actual sea runs. What causes such a discrepancy has not been clarified to date. It is conceivable that 1) a small trim angle (such as 1 ~ 2°) existing at actual sea runs might have caused a change in boundary layer velocity profile, or 2) the boundary layer may be different between the water tunnel and unbounded flow environment so that the pumpjet performance is substantially affected. It should be noted that the utilization of the boundary layer is an advantage in obtaining the pumpjet's high efficiency on one hand but it is a disadvantage in causing many difficult problems on the other hand.

* Some pumpjet rotors are produced by investment casting process so that the fabrication accuracy cannot be expected to be high.

The turning capability of the underwater vehicle thrusted with a pumpjet is said to be inferior to that with, e.g., a counter-rotating propeller. The reason for such inferior turning capability seems also attributable to the utilization of the wake flow; when the vehicle turns, the boundary layer substantially changes. The pumpjet seems to lose a considerable thrust capability due to the change of boundary layer velocity profile, resulting in a poor turning capability.

Another problem area in the pumpjet lies in the pumpjet design method. The only design method developed to date and used is a two-dimensional graphic method combined with experimental data of Bruce, et al. (1977) despite the fact that the pumpjet experiences a three-dimensional flow. Based on the momentum theorem applied to the cascade configuration, the blade sectional pressure increase Δp is given

$$\Delta p = K\, V_m \cdot \Delta V_\theta \qquad (1.1)$$

where

Δp = local pressure increase through the rotor,

V_m = meridional velocity,

ΔV_θ = circumferential velocity, and

K = a constant determined by the cascade configuration.

This two-dimensional momentum theory indicates that, in order to generate a certain pressure increase at a blade section, only the amount of total flow deflection in the circumferential direction (between the inlet and exit) counts, see Figure 1-6. In this method once the sectional blade leading edge and trailing edge angles are determined, then the rest of the blade section can be arbitrarily determined by connecting these predetermined leading and trailing edges, e.g., anglewise smoothly.

One of the obvious problems in this graphic method arises from the fact that the flow coming into the cascade blade cannot exactly follow the blade camber, but substantially deviates from it. What is required therefore is a camber correction, the amount of which depends upon the cascade geometry. Unfortunately, a typical pumpjet solidity* near the hub is larger than 2.0 and therefore the camber correction required there becomes as much as 5 times in terms of lift coefficient. It means that the camber graphically constructed should be deformed until the lift coefficient increases by 5 times that graphically obtained. This correction is made semi-empirically based on limited numbers of existing experimental data for cascade blade flows. In this sense, therefore, this graphical method is useless for the blade design near the hub and it can be said that the final design is almost entirely dependent upon these empirical data.

* Solidity is defined as a ratio of blade chord length to blade spacing measured normal to the axial direction and the high solidity means more blade packed cascade.

2.0 OBJECTIVES

The objectives of the work to be conducted under the GHR program are therefore:

1) to develop a more reliable and accurate pumpjet design method based on a three-dimensional pump or propeller design theory and then

2) to improve the pumpjet performance characteristics.

The characteristics to be improved include:

a) the susceptibility to flow disturbance and rotor's deformation due to fabrication inaccuracy,

b) the discrepancy problem between the water tunnel test results and high speed sea runs and

c) the poor turning capability.

3.0 METHODOLOGY SELECTION FOR A THREE-DIMENSIONAL PUMPJET DESIGN

3.1 REQUIREMENTS AND CANDIDATES

There exist several possible approaches which can incorporate three-dimensionality into pumpjet design procedure. However, the following aspects should be considered in selecting such a methodology:

1) Moderate three-dimensionality
   A pumpjet is usually installed astern of underwater vehicle hull where the hull shape has a negative slope of tapering shape. Although this provides three-dimensional flow characteristics, its three-dimensionality is rather mild, unlike that in radial pump cases.

2) Capability of determining detailed blade profile shapes as well as pressure distribution
   In the previous two-dimensional graphic method Bruce, et al. (1974), the blade profile shape was graphically determined for meeting the head generation requirement. It is mainly for this reason that the method failed to check the possibility of flow separation after the blade was designed. A new method to be developed in this research work should be the one with which the detailed pressure distribution or velocity distribution on the blade can be determined.

3) Accurate loading determination supported by experiments
   When the sectional loading is determined analytically in the course of designing a pumpjet, it is usually quite inaccurate since such loading substantially changes due to the effect of adjacent blades. It is therefore necessary for the new method to incorporate the cascade effect into design procedure, or to use an empirical approach to increase such accuracy.

With these features taken into consideration, the following three candidate methods are compared in Section 3.2:

Method I: Katsanis' Quasi-Three-Dimensional Method

Method II: Blade-Through Flow with Blade-to-Blade Flow Method

Method III: Singularity Distribution Method

for which simple explanation will be given in the following.

Method I: Katsanis' (1964) Quasi-Three-Dimensional Method

In this method it is first assumed that a mean stream surface from hub to shroud between blades is known in advance. On this stream surface a two-dimensional solution for the velocity and pressure distributions is obtained. Then, an approximate calculation of the blade surface velocities is made. This method is based on an equation for the velocity gradient along an arbitrary quasi-orthogonal rather than the normal to the streamline. Since the solution is obtained on this quasi-orthogonal line, in this method, an iteration procedure needed in the previous orthogonal-line methods can be eliminated and a solution can be obtained in a single computer run.

Method II: Blade-Through Flow with Blade-to-Blade Flow Method

The blade-through flow is first obtained by, e.g., Streamline Curvature Method (SCM). Once the stream surface is found, it is mapped to a two-dimensional plane so that the blades cut through by the stream surface become a row of blades, i.e., cascade on a plane. On this cascade configuration, the blade-to-blade flow will be solved. Difficulty in doing this lies in the fact that the governing equation is not a Laplace equation any more on this two-dimensional plane, but a Poisson equation due to the deviation of stream surface from a perfect cylinder. In order to account for such deviation into the two-dimensional flow, appropriate source/sink and vortices should be distributed over the entire flow field. This, in turn, results in the change of blade camber shape. The design procedure relies on an iteration scheme.

Method III: Singularity Distribution Method

The method is similar to that used in design of conventional propellers, see, e.g., the work by Kerwin and Leopold (1964). The differences in velocities between the pressure and suction sides of rotor blade can be represented by distributions of singularities such as source/sink and vortex. The strengths of such singularities are determined by satisfying the boundary conditions on the blade surface as well as those at infinity. The methodology is described in the paper of Kerwin and Leopold (1964) in detail.

The disadvantage of the method lies in the computational complexity and instability. Furthermore, this type of method is suitable for design of devices used in the open field, but not so for those used in the internal flow since it does not take advantage of confined flow configuration available for the latter case.

3.2 COMPARISON AND SELECTION

Table 3-1 provides qualitative evaluation on three candidate methods described in the previous section over various hydrodynamic, numerical and design aspects. As seen from this table, a combination of blade-through method with blade-to-blade flow seems to have an advantage over the other two methods. Particularly, the method has the capability of determining detailed blade profile shape as well as loading and velocity/pressure distribution with accuracy verified by existing cascade experimental data. It is for this reason that the blade-through flow with blade-to-blade flow method has been selected as a basic concept for developing a three-dimensional pumpjet design method.

Similar methods already exist for design of quasi-axial pumps and compressors. However, those methods have many inadequate features in their design procedure. Furthermore,

it is assumed in these design methods that the incoming flow is more or less uniform, unlike the pumpjet where the rotor should be designed for highly retarded velocity distribution due to viscous boundary layer on the hull. The following section describes the blade-through flow (BT) with blade-to-blade flow (BTB) method with various aspects of modifications and improvement necessary for developing the pumpjet design method.

4.0 SELECTED DESIGN METHOD--BLADE-THROUGH/ BLADE-TO-BLADE METHOD

Design of a pumpjet for an underwater vehicle requires preliminary information on the vehicle including its geometry and hydrodynamic drag coefficient. Furthermore, most importantly, the velocity profile at an upstream reference section should be obtained either analytically or experimentally. Any error in the velocity profile would result in a pumpjet of lower efficiency or failure of the pumpjet meeting the specifications at the design point. In the present study, it is assumed that this velocity profile is given at a goal speed or at the corresponding Reynolds number.

The first step for design of a pumpjet (see Figure 4-1) is to determine the shroud intake diameter. From the viewpoint of cavitation, the maximum and minimum shroud diameter to prevent cavitation must exist. If it is too large, the rotor blade tip speed becomes too high so that cavitation occurs. On the other hand, if it is too small, the rotation speed must be increased to generate the required head so that the chance of cavitation inception also increases. Another aspect of determining the shroud diameter stems from consideration of the overall propulsive efficiency. The equation for global momentum balance should be able to determine an efficiency-optimum shroud diameter for the given velocity profile and vehicle drag. The detailed mathematical formulation and sample calculations will be given in Section 4.1.

Once the shroud diameter is determined, the streamline will be calculated by using the streamline curvature method (SCM). In this calculation, the loading distribution on the rotor and blade thickness must be assumed in advance. One of the major concerns in using the existing streamline curvature method lies in the fact that SCM may only be used for relatively uniform incoming flow, but may generate a sub-

stantial error for a thick wake flow, i.e., highly retarded flow due to the viscous boundary layer on the vehicle hull. Detailed mathematical formulation and sample calculations are presented in Section 4.2. Also included are discussions regarding the problems of application of conventional SCM to the thick wake flow.

The next step of the design method is to map the stream tube or surface calculated by SCM onto a plane so that the rotor blades are mapped into cascade configuration. If the stream surface is totally cylindrical shape, the governing equation to be used for the cascade analysis will be a Laplace equation. Unfortunately, the stream surface is of three-dimensional cone shape in general for the tail cone section of the underwater vehicle. The field governing equation now becomes a Poisson equation, for which the results of powerful potential theory analysis are no more applicable. A method of correcting the effect of the Poisson equation on the potential theory results is introduced to modify the blade profile shape obtained in the potential theory. In choosing the blade profile shape, the experimental data are used to ensure that there is no chance of flow separation due to overloading on the blade. Furthermore, based on the calculated velocity along the blade, the cavitation inception is checked. If there exists a chance of either flow separation or cavitation, the loading distribution from hub to tip should be changed. If such a change is made, and/or thickness of blades is changed, the streamline curvature method should be used again to determine the new location of streamline or stream surface. This iterative procedure will be repeated until an overall convergent solution is obtained. Section 4.3 describes the technical approach to be used for the blade-to-blade flow analysis.

4.1 PUMPJET GLOBAL HYDRODYNAMICS

It is a well-known fact that the pumpjet utilizes the tail-cone low-energy, boundary layer flow in order to achieve its high efficiency. It means that the optimum* pumpjet design depends entirely upon the incoming flow velocity profile.

Figure 4-2 shows a schematic diagram of an underwater vehicle tail cone/pumpjet flow. (1) and (7) in Figure 4-2 are considered to be the upstream and downstream reference stations, respectively, where it is assumed that the free-stream static pressure exists, whereas (2) and (3) are the rotor inlet and exit stations.

4.1.1 Calculation of Thrust Force

The thrust force, T, due to the pumpjet work can be determined by applying the momentum equation to the control volume enclosed by stations (1), (7) and the stagnation streamline (see Figure 4-2).

$$T = \int_{r_{H7}}^{r_{T7}} d\dot{m}_7 \cdot V_7(r)\cos\theta_7 \; - \int_{r_{H1}}^{r_{T1}} d\dot{m}_1 \cdot V_1(r)\cos\theta_1 \qquad (4.1.1\text{-}1)$$

$$\left.\begin{aligned} \text{where } d\dot{m}_7 &= \rho 2\pi r V_7(r)\cos\theta_7\, dr \\ d\dot{m}_1 &= \rho 2\pi r V_1(r)\cos\theta_1\, dr \end{aligned}\right\} \qquad (4.1.1\text{-}2)$$

$V_1(r)$, $V_7(r)$ = meridional flow velocities at (1) and (7), respectively.

θ_1, θ_7 = meridional flow angles at (1) and (7), respectively.

Note *By "optimum" pumpjet design it means that of proving the maximum propulsion efficiency.

Therefore

$$T = \int_{r_{H7}}^{r_{T7}} \rho 2\pi r V_7^2(r)\cos^2\theta_7\, dr \; - \int_{r_{H1}}^{r_{T1}} \rho 2\pi r V_1^2(r)\cos^2\theta_1\, dr \qquad (4.1.1\text{-}3)$$

Defining the following quantities,

$$\frac{\bar{V}_7}{V_\infty} = \frac{\int_{r_{H7}/r_B}^{r_{T7}/r_B} \left(\frac{V_7(r)}{V_\infty}\right)^2 \frac{r}{r_B}\cdot\cos\theta_7\, d\left(\frac{r}{r_B}\right)}{\int_{r_{H7}/r_B}^{r_{T7}/r_B} \frac{V_7(r)}{V_\infty}\frac{r}{r_B}\cos\theta_7\cdot d\left(\frac{r}{r_B}\right)} \qquad (4.1.1\text{-}4)$$

$$\frac{\bar{V}_1}{V_\infty} = \frac{\int_{r_{H1}/r_B}^{r_{T1}/r_B} \left(\frac{V_1(r)}{V_\infty}\right)^2 \frac{r}{r_B}\cos\theta_1\, d\left(\frac{r}{r_B}\right)}{\int_{r_{H1}/r_B}^{r_{T1}/r_B} \frac{V_1(r)}{V_\infty}\frac{r}{r_B}\cos\theta_1\, d\left(\frac{r}{r_B}\right)} \qquad (4.1.1\text{-}5)$$

and normalizing T, Eqn. (4.1.1-3) becomes

$$C_T = \frac{T}{\frac{1}{2}\rho V_\infty^2 \cdot A_B}$$

$$= \frac{\int_{r_{H7}}^{r_{T7}} \rho 2\pi r V_7^2(r)\cos^2\theta_7\, dr \; - \int_{r_{H1}}^{r_{T1}} \rho 2\pi r V_1^2(r)\cos^2\theta_1\, dr}{\frac{1}{2}\rho V_\infty^2 \pi r_B^2}$$

$$= 4\left[\int_{r_{H7}/r_B}^{r_{T7}/r_B} \left(\frac{V_7(r)}{V_\infty}\right)^2 \left(\frac{r}{r_B}\right)\cos^2\theta_7\, d\left(\frac{r}{r_B}\right) - \int_{r_{H1}/r_B}^{r_{T1}/r_B} \left(\frac{V_1(r)}{V_\infty}\right)^2 \left(\frac{r}{r_B}\right)\cos^2\theta_1\, d\left(\frac{r}{r_B}\right)\right]$$

$$= 2 \left(\frac{\bar{V}_7}{V_\infty} \cos\theta_7 - \frac{\bar{V}_1}{V_\infty} \cos\theta_1 \right) C_m \qquad (4.1.1\text{-}6)$$

where the mass conservation equation below has been used;

$$C_m = C_{m1} = C_{m7} \qquad (4.1.1\text{-}7)$$

$$\dot{m}_1 = \int_{r_{H1}}^{r_{T1}} \rho 2\pi r V_1(r) \cos\theta_1 \, dr \qquad (4.1.1\text{-}8)$$

$$\dot{m}_7 = \int_{r_{H7}}^{r_{T7}} \rho 2\pi r V_7(r) \cos\theta_7 \, dr \qquad (4.1.1\text{-}9)$$

$$C_{m1} = \frac{\dot{m}_1}{\rho V_\infty \pi r_B^2} = 2 \int_{r_{H1}/r_B}^{r_{T1}/r_B} \frac{V_1(r)}{V_\infty} \cdot \frac{r}{r_B} \cos\theta_1 \, d\left(\frac{r}{r_B}\right) \qquad (4.1.1\text{-}10)$$

$$C_{m7} = \frac{\dot{m}_7}{\rho V_\infty \pi r_B^2} = 2 \int_{r_{H7}/r_B}^{r_{T7}/r_B} \frac{V_7(r)}{V_\infty} \frac{r}{r_B} \cos\theta_7 \cdot d\left(\frac{r}{r_B}\right) \qquad (4.1.1\text{-}11)$$

Let's define

$$\frac{\Delta\bar{V}_a}{V_\infty} = \frac{\bar{V}_7 \cos\theta_7}{V_\infty} - \frac{\bar{V}_1 \cos\theta_1}{V_\infty} , \qquad (4.1.1\text{-}12)$$

then we obtain, from (4.1.1-6)

$$C_T = 2 \cdot \left(\frac{\Delta\bar{V}_a}{V_\infty} \right) \cdot C_m \qquad (4.1.1\text{-}13)$$

Note that

$$C_m = 2 \cdot \left(\frac{\bar{V}_1}{V_\infty} \right) \frac{A_1}{A_B} \qquad (4.1.1\text{-}14)$$

where

$$\frac{\bar{V}_1}{V_\infty} = \frac{\int_{r_{H1}/r_B}^{r_{T1}/r_B} \frac{V_1(r)}{V_\infty} \left(\frac{r}{r_B}\right) \cos\theta_1 \, d\left(\frac{r}{r_B}\right)}{\int_{r_{H1}/r_B}^{r_{T1}/r_B} \left(\frac{r}{r_B}\right) \cos\theta_1 d\left(\frac{r}{r_B}\right)} \qquad (4.1.1\text{-}15)$$

4.1.2 Relationship Between Pump Head and Thrust

The hydraulic head of the pump $\tilde{H}_R$ is given

$$\frac{\tilde{H}_R}{V_\infty^2/2g} = \frac{2\int_{r_{H3}/r_B}^{r_{T3}/r_B} \frac{V_3}{V_\infty} \frac{U}{V_\infty} \frac{V_{\theta 3}}{V_\infty} \frac{r}{r_B} \frac{1}{\cos\theta_3} d\left(\frac{r}{r_B}\right)}{\int_{r_{H3}/r_B}^{r_{T3}/r_B} \frac{V_3}{V_\infty} \frac{r}{r_B} \frac{1}{\cos\theta_3} d\left(\frac{r}{r_B}\right)} \qquad (4.1.2\text{-}1)$$

where $V_3(r)$, $V_{\theta 3}(r)$ = meridional and circumferential velocities at station (3), respectively.

With the hydraulic efficiency η_R introduced, the actual head generated in the fluid is $\tilde{H}$,

$$\tilde{H} = \eta_R \cdot \tilde{H}_R \qquad (4.1.2\text{-}2)$$

where $\tilde{H}$ can be defined

$$\frac{\tilde{H}}{V_\infty^2/2g} = \left(\frac{\tilde{V}_7}{V_\infty}\right)^2 - \left(\frac{\tilde{V}_1}{V_\infty}\right)^2 + K_1\left(\frac{\tilde{V}_1}{V_\infty}\right)^2 \qquad (4.1.2\text{-}3)$$

$$\text{where } \left(\frac{\tilde{V}_7}{V_\infty}\right)^2 = \frac{\int_{r_{H7}/r_B}^{r_{T7}/r_B} \left(\frac{V_7(r)}{V_\infty}\right)^3 \frac{r}{r_B} \cos\theta_7 d\left(\frac{r}{r_B}\right)}{\int_{r_{H7}/r_B}^{r_{T7}/r_B} \left(\frac{V_7(r)}{V_\infty}\right) \frac{r}{r_B} \cos\theta_7 d\left(\frac{r}{r_B}\right)} \qquad (4.1.2\text{-}4)$$

$$\left(\frac{\tilde{V}_1}{V_\infty}\right)^2 = \frac{\int_{r_{H1}/r_B}^{r_{T1}/r_B} \left(\frac{V_1(r)}{V_\infty}\right)^3 \frac{r}{r_B} \cos\theta_1 \, d\left(\frac{r}{r_B}\right)}{\int_{r_{H1}/r_B}^{r_{T1}/r_B} \left(\frac{V_1(r)}{V_\infty}\right) \frac{r}{r_B} \cos\theta_1 \, d\left(\frac{r}{r_B}\right)} \quad , \qquad (4.1.2\text{-}5)$$

K_1 = head loss coefficient between station (1) and (7) (but mostly inlet loss and see Appendix for determining K_1).

Since

$$\bar{\Delta V}_m = \bar{V}_7 - \bar{V}_1 \qquad (4.1.2\text{-}6)$$

and $\bar{\Delta V}_m$ can be approximated as $\bar{\Delta V}_m \simeq \tilde{V}_7 - \tilde{V}_1$, Eqn. (4.1.2-3) becomes

$$\frac{H}{V_\infty^2/2g} = 2 \frac{\bar{\Delta V}_m}{V_\infty} \cdot \frac{\tilde{V}_1}{V_\infty} + \left(\frac{\bar{\Delta V}_m}{V_\infty}\right)^2 + K_1 \left(\frac{\tilde{V}_1}{V_\infty}\right)^2 . \qquad (4.1.2.7)$$

From Eqns. (4.1.1-12) and (4.1.2-7),

$$\frac{\bar{\Delta V}_m}{V_\infty} = \frac{\frac{\bar{\Delta V}_a}{V_\infty} + \frac{\bar{V}_1}{V_\infty}(\cos\theta_1 - \cos\theta_7)}{\cos\theta_7} \qquad (4.1.2\text{-}8)$$

4.1.3 Power Calculation

The power to be used on the pumpjet rotor shaft can be calculated by integrating the product of the local head and the local mass flow rate over the entire duct flow,

$$P = \int \rho g \Delta Q H \ ,$$

or in terms of the power coefficient

$$C_P = \frac{P}{\frac{1}{2}\rho V_\infty^3 A_B} = \frac{\int \rho g \Delta Q H}{\frac{1}{2}\rho V_\infty^3 \pi r_B^2}$$

$$= \frac{\rho g \int_{r_{H3}}^{r_{T3}} \frac{V_{\theta 3} \cdot U}{g} \cdot V_3(r) 2\pi r \frac{1}{\cos\theta_3} dr}{\frac{1}{2}\rho V_\infty^3 \pi r_B^2}$$

or

$$C_P = 4 \int_{r_{H3}/r_B}^{r_{T3}/r_B} \left(\frac{V_{\theta 3}}{V_\infty}\right)\left(\frac{U}{V_\infty}\right)\left(\frac{V_3(r)}{V_\infty}\right)\frac{r}{r_B}\frac{1}{\cos\theta_3} d\left(\frac{r}{r_B}\right). \qquad (4.1.3\text{-}1)$$

From (4.1.2-1),

$$C_P = 2 \frac{\tilde{H}_R}{V_\infty^2/2g} \cdot \int_{r_{H3}/r_B}^{r_{T3}/r_B} \frac{V_3}{V_\infty} \frac{r}{r_B} \frac{1}{\cos\theta_3} d\left(\frac{r}{r_B}\right)$$

$$= \frac{\tilde{H}_R}{V_\infty^2/2g} \cdot C_m ,$$

or

$$C_P = \frac{1}{\eta_R} \cdot \frac{\tilde{H}}{V_\infty^2/2g} \cdot C_m \qquad (4.1.3\text{-}2)$$

Therefore, the propulsive efficiency η_P can be calculated from the following definition:

$$\eta_P = \frac{C_T}{C_P} \qquad (4.1.3\text{-}3)$$

4.1.4 Procedure of Calculating Propulsive Efficiency with $V_1(r)$, etc. given and Sample Results

Now all tools for calculating the propulsive efficiency η_P with $V_1(r)$ given are provided. The principal equations to be used will be Eqns. (4.1.1-13), (4.1.2-6), (4.1.2-8),

(4.1.3-2), and (4.1.3-3). A flow chart describing the calculation procedure is given in Figure 4-3.

Sample velocity profiles, $V_1(r)$ and $V_2(r)$, are shown in Figures 4-4 and 4-5. The flow angles, θ_1, θ_2 and θ_7, can be obtained from the drawings of a typical underwater vehicle tail cone profile. The head loss coefficient, K_1, can be calculated from the formula given in Appendix A with the velocity distributions and pressure distributions both at stations (1) and (2), which are also given in Figures 4-4 and 4-5.

Figures 4-6 to 4-7 show the results of calculations made for various parameters, including the shroud opening diameter, r_1/r_B, the exit jet flow angle θ_7, and flow velocity amplification factor. The design values of r_1/r_B and flow amplification factor are known, i.e.,

$$(r_1/r_B)_D = .93.$$

Flow Amplification Factor = 1

but that of θ_7 is not known except for the fact that the average geometric angle of the shroud and tail cone angle at exit is about 11°. Theoretically, however, the jet coming out from the shroud exit with 11° should align itself in the direction of the body axis, indicating that θ_7 could be zero. The present calculations were therefore made for θ_7 = 0°, 5°, 8° and 11°.

The shroud opening, r_1/r_B, was also varied in the present analysis in order to determine the optimum shroud opening radius in terms of efficiency. Also changed was the incoming flow velocity amplitude to investigate a possibility of pumpjet efficiency improvement in combination with the tail cone flow pattern change.

The pump hydraulic efficiency η_R for this type of pump, used in the analysis, is about 89°, which is the measured value by many pump makers.

Figures 4-6 to 4-8 show the calculated propulsive efficiencies as a function of the shroud opening r_1/r_B with the flow amplification factor as a parameter for $\theta_7 = 0°$, 5° and 11°, respectively. As can be seen from these figures, the efficiency curve has the maximum value at an r_1/r_B value specific for the conditions used.

Figure 4-6 shows that the efficiency at the design condition should be 88.4% when $\theta_7 = 0°$ is assumed. The design shroud opening, $r_1/r_B = .93$, is slightly on the smaller side than that for the maximum efficiency. The maximum efficiency of 88.8% can be obtained at a slightly larger shroud radius. i.e., $r_1/r_B = .95$. Also seen from Figure 4-6 is the fact that the smaller the incoming flow velocity, the larger the maximum propulsive efficiency. This indicates that, if the incoming velocity amplitude at the tail cone area can be reduced by some means, the propulsive efficiency of the pumpjet is substantially increased.

It should also be remembered that the actual efficiency achieved is 76.9%, much lower than any of the values calculated here.

As θ_7 increases, the efficiency curves shift to the lower efficiency side, see Figures 4-6 to 4-8. This is naturally expected since the jet thrusting force is not effectively utilized as θ_7 increases.

It may also be coincidental, as seen in Figure 4-8, that if $\theta_7 = 11°$ is used as obtained from the pumpjet exit geometry, the current shroud opening, $r_1/r_B = .93$, is the optimum selection for providing the maximum efficiency, 82.9%, smaller than that of the original design. It should be pointed out that if $\theta_7 = 11°$ is the true exit jet flow angle, an increase in the shroud radius for alleviating the flow separation problem may cost a substantial efficiency loss (see Figure 4-8). On the other hand, if $\theta_7 = 0°$ is the true value, a moderate increase (e.g., 2%) in the shroud

radius will increase the efficiency in addition to the efficiency gained due to the suppression of the flow separation. However, again the penalty exists when the amount of shroud radius increase exceeds more than 4%.

Figure 4-9 summarizes the present calculations in terms of the maximum propulsive efficiency with θ_7 and the flow amplification factor as parameters. It is shown that a substantial efficiency improvement may be achieved by

1) reducing the incoming flow velocity amplitude by modifying the tail cone profile shape and thus changing the boundary layer flow,

2) choosing the optimum shroud opening radius depending on the flow conditions (see also Figures 4-6 to 4-8),

3) redirecting the jet flow at the shroud exit as close to the body axis as possible, if the jet flow of the current design is not.

4.2 BLADE-THROUGH FLOW ANALYSIS - STREAMLINE CURVATURE METHOD (SCM)

4.2.1 Mathematical Formulation

From the definition of entropy, S, in the second law of thermodynamics, the following relationship is obtained for a reversible transformation, i.e.,

$$T\nabla S = \nabla Q \qquad (4.2.1\text{-}1)$$

where T is the temperature and ∇Q is the amount of heat the system under consideration receives. On the other hand, the first law of thermodynamics says

$$\nabla E = \nabla Q + \nabla W \qquad (4.2.1\text{-}2)$$

where E is the internal energy and W is the work performed on the fluid. Since $\nabla W = -p\nabla v$, (4.2.1-2) becomes

$$\nabla E = \nabla Q - p\nabla v$$

$$= \nabla Q - p\nabla\left(\frac{1}{\rho}\right) \qquad (4.2.1\text{-}3)$$

where v is the specific volume of fluid and, in terms of fluid density, ρ, $v = 1/\rho$. The definition of enthalpy, H, is given by

$$H = \frac{1}{2} u^2 + E + \frac{p}{\rho} + \Psi \qquad (4.2.1\text{-}4)$$

where u is the amplitude of flow velocity and Ψ is the potential energy. Gradient of H yields

$$\nabla H = \nabla\left(\frac{1}{2} u^2 + \Psi\right) + \nabla E + \frac{1}{\rho} \nabla p + p\nabla\left(\frac{1}{\rho}\right)$$

From the above equation and Eqn. (4.2.1-3),

$$\nabla H = T\nabla S + \nabla\left(\frac{1}{2} u^2 + \Psi\right) + \frac{1}{\rho} \nabla p \qquad (4.2.1\text{-}5)$$

The steady-state momentum theorem gives

$$\rho \underline{u} \cdot \nabla \underline{u} = -\nabla p - \rho \nabla \Psi \qquad (4.2.1\text{-}6)$$

where an assumption has been made that $-\nabla\Psi = \underline{F}$, where $\underline{F}$ is an external force. By using a vector identity, $\underline{u} \times (\nabla \times \underline{u}) = \frac{1}{2} \nabla u^2 - \underline{u} \cdot \nabla \underline{u}$, Eqn. (4.2.1-6) is now written

$$\underline{u} \times (\nabla \times \underline{u}) = \frac{1}{2} \nabla u^2 + \nabla\Psi + \frac{1}{\rho} \nabla p$$

or
$$\underline{u} \times \underline{\omega} = \nabla\left(\frac{u^2}{2} + \Psi\right) + \frac{1}{\rho} \nabla p \qquad (4.2.1\text{-}7)$$

where $\underline{\omega} = \nabla \times \underline{u}$. Substituting Eqn. (4.2.1-5) into (4.2.1-7) gives

$$\underline{u} \times \underline{\omega} = \nabla H - T\nabla S, \qquad (4.2.1\text{-}8)$$

a relation first found by Crocco (1937), which will be used to derive the formula used for SCM hereafter.

By using the cylindrical coordinate system (r,θ,z), the velocity components of $\underline{u}$ are defined by

$$\underline{u} = (u_r, u_\theta, u_z). \qquad (4.2.1.9)$$

Thus, the components of vortex term $\underline{\omega}$ is written

$$\text{(a)}\quad \underline{\omega}_r = (\nabla \times \underline{u})_r = \frac{1}{r}\left(\frac{\partial u_z}{\partial \theta} - \frac{\partial r u_\theta}{\partial z}\right)$$

$$\text{(b)}\quad \underline{\omega}_\theta = (\nabla \times \underline{u})_\theta = \frac{\partial u_r}{\partial z} - \frac{\partial u_z}{\partial r} \qquad (4.2.1\text{-}10)$$

$$\text{(c)}\quad \underline{\omega}_z = (\nabla \times \underline{u})_z = \frac{1}{r}\left(\frac{\partial r u_\theta}{\partial r} - \frac{\partial u_r}{\partial \theta}\right)$$

By introducing a direction m, defined by, (see also Fig. 4-10)

$$\text{(a)}\quad dm : dr : dz = u_m : u_r : u_z$$

$$\text{(b)}\quad u_m^2 = u_r^2 + u_z^2$$

$$\text{(c)}\quad \tan\phi = u_r/u_z \qquad (4.2.1\text{-}11)$$

$$\text{(d)}\quad u_r = u_m \sin\phi$$

$$\text{(e)}\quad u_z = u_m \cos\phi \ ,$$

it becomes evident that the m-direction is the "meridional direction" or on the projection of streamline in the r-z plane. The directional derivative with respect to m then becomes

$$\text{(a)}\quad u_m \frac{\partial}{\partial m} = u_r \frac{\partial}{\partial r} + u_z \frac{\partial}{\partial z}$$

$$\text{(b)}\quad \frac{\partial}{\partial m} = \frac{\partial r}{\partial m}\frac{\partial}{\partial r} + \frac{\partial z}{\partial m}\frac{\partial}{\partial z}$$

$$= \sin\phi \frac{\partial}{\partial r} + \cos\phi \frac{\partial}{\partial z} \qquad (4.2.1\text{-}12)$$

where (4.2.1-11) has been used.

Furthermore, the θ-component of the Crocco equation (4.2.1-8) gives

$$\frac{u_z}{r}\left(\frac{\partial u_z}{\partial \theta} - \frac{\partial r u_\theta}{\partial z}\right) - \frac{u_r}{r}\left(\frac{\partial r u_\theta}{\partial r} - \frac{\partial u_r}{\partial \theta}\right)$$

$$= \frac{1}{r}\left(\frac{\partial H}{\partial \theta} - T\frac{\partial S}{\partial \theta}\right). \qquad (4.2.1\text{-}13)$$

Under the assumption of axisymmetricity,

$$\frac{\partial H}{\partial \theta} = 0$$

$$T\frac{\partial S}{\partial \theta} = 0 \ ,$$

so that Eqn. (4.2.1.-13) becomes

$$u_r \frac{\partial u_r}{\partial \theta} + u_z \frac{\partial u_z}{\partial \theta} = u_r \frac{\partial r u_\theta}{\partial r} + u_z \frac{\partial r u_\theta}{\partial z}$$

or $$\frac{1}{2} \cdot \frac{\partial}{\partial \theta}\left(u_r^2 + u_z^2\right) = u_m \frac{\partial r u_\theta}{\partial m}$$

Using (4.2.1-11b),

$$\frac{\partial u_m}{\partial \theta} = \frac{\partial r u_\theta}{\partial m} \qquad (4.2.1\text{-}14)$$

It is now ready to perform a coordinate transform of Eqn. (4.2.1-10) by using Eqns. (4.2.1-11), (4.2.1-12) and (4.2.1-14). The result is

$$\text{(a)} \quad \underline{\omega}_r = (\nabla \times \underline{u})_r = \frac{\tan\phi}{r}\left[\frac{\partial r u_\theta}{\partial r} - \sin\phi \frac{\partial r u_\theta}{\partial m} - u_m \cos\phi \frac{\partial \phi}{\partial \theta}\right]$$

$$\text{(b)} \quad \underline{\omega}_\theta = (\nabla \times \underline{u})_\theta = \frac{1}{u_m \cos\phi}\left[u_m^2\left(\frac{\sin\phi}{u_m}\frac{\partial u_m}{\partial m} - \frac{\cos\phi}{r_m}\right) - \frac{1}{2}\frac{\partial u_m^2}{\partial r}\right] \qquad (4.2.1\text{-}15)$$

$$\text{(c)} \quad \underline{\omega}_z = (\nabla \times \underline{u})_z = \frac{1}{r}\left[\frac{\partial r u_\theta}{\partial r} - \sin\phi \frac{\partial r u_\theta}{\partial m} - u_m \cos\phi \frac{\partial \phi}{\partial \theta}\right]$$

where r_m is the radius of curvature of the meridional streamline projection, defined by

$$\frac{1}{r_m} = -\frac{\partial \phi}{\partial m} \tag{4.2.1-16}$$

Further application of axisymmetricity to Eqn. (4.2.1-15) yields

$$\text{(a)}\quad \underline{\omega}_r = (\nabla \times \underline{u})_r = \frac{\tan\phi}{r}\left(\frac{\partial r u_\theta}{\partial r}\right)$$

$$\text{(b)}\quad \underline{\omega}_\theta = (\nabla \times \underline{u})_\theta = \frac{1}{u_m \cos\phi}\left[u_m^2\left(\frac{\sin\phi}{u_m}\frac{\partial u_m}{\partial m} - \frac{\cos\phi}{r_m}\right) - \frac{1}{2}\frac{\partial u_m^2}{\partial r}\right] \tag{4.2.1-17}$$

$$\text{(c)}\quad \underline{\omega}_z = \frac{1}{r}\left(\frac{\partial r u_\theta}{\partial r}\right)$$

where the following relations

$$\frac{\partial \phi}{\partial \theta} = 0$$

$$\frac{\partial r u_\theta}{\partial m} = \frac{\partial u_m}{\partial \theta} = 0$$

have been applied.

The right-hand side of Eqn. (4.2.1-8) becomes ∇H under the assumption of adiabatic process for the fluid to go through the pump channel.

Now, it is ready to write the r-component of Eqn. (4.2.1-8) for the meridional flow velocity and the final form is shown after some rearrangement:

$$\frac{\partial u_m^2}{\partial r} + 2\left(-\frac{\sin\phi}{u_m}\frac{\partial u_m}{\partial m} + \frac{\cos\phi}{r_m}\right) u_m^2 = 2\left(\frac{\partial H}{\partial r} - \frac{u_\theta}{r}\frac{\partial r u_\theta}{\partial r}\right) \tag{4.2.1-18}$$

Eqn. (4.2.1-18) can be written as

$$\frac{\partial u_m^2}{\partial r} + P(r)\, u_m^2 = T(r) \qquad (4.2.1\text{-}19)$$

where

$$P(r) = 2\left(-\frac{\sin\phi}{u_m}\frac{\partial u_m}{\partial m} + \frac{\cos\phi}{r_m}\right)$$

$$T(r) = 2\left(\frac{\partial H}{\partial r} - \frac{u_\theta}{r}\frac{\partial r u_\theta}{\partial r}\right) \qquad (4.2.1\text{-}20)$$

In Eqns. (4.2.1-18) - (4.2.1-20), the first term of P(r), i.e., $\sin\phi/u_m \cdot \partial u_m/\partial m$, will provide some difficulty in numerical computations since it is related to the derivatives with respect to "m". The basic philosophy of the streamline curvature method is to express the meridional velocity in terms of "r" and "r-derivatives" so that u_m can be solved in the direction of r only. This feature will be of advantage in numerical computations since the derivatives with respect to "m" are not needed and thus the m-directional control points do not have to be taken in fine increments. Fortunately, $\sin\phi/u_m \cdot \partial u_m/\partial m$ can be expressed in terms of r by using the continuity equation

$$\frac{\partial u_z}{\partial z} + \frac{1}{r}\frac{\partial r u_r}{\partial r} + \frac{1}{r}\frac{\partial u_\theta}{\partial \theta} = 0.$$

Again, applying the axisymmetric assumption and Eqns. (4.2.1-11), (4.2.1-12) and (4.2.1-16), the following relation is obtained

$$\frac{\sin\phi}{u_m}\cdot\frac{\partial u_m}{\partial m} = -\left[\frac{\sin^2\phi}{r}\left(1 + \frac{r}{r_m\cos\phi}\right) + \tan\phi\cdot\frac{\partial\phi}{\partial r}\right] \qquad (4.2.1\text{-}21)$$

The basic equation for the streamline curvature method, i.e., Eqn. (4.2.1-18), is expressed in terms of "r" except for the radius of curvature, r_m, so that it can be readily solved numerically. The only problem remaining is that

$u_m(r)$ cannot be uniquely determined. This problem can be resolved by applying the mass conservation equation

$$2\pi \int_{r_h}^{r_s} K_b \cdot \rho r \, u_m(r) \cos\phi_q \, dr = \dot{G} \qquad (4.2.1\text{-}22)$$

where K_b is the blockage factor due to the blade displacement thickness as well as that of the boundary layer, and ϕ_q is the angle between the line of integration (called "q-line" hereafter) and the line normal to the streamline. With this, the mathematical formulation for the streamline curvature method (SCM) is completed. In what follows, the numerical solution method for SCM will be described in detail.

4.2.2 Solution Method

Since Eqns. (4.2.1-18) and (4.2.1-22) are highly nonlinear for u_m, only an iterative procedure depending on numerical analysis is a possible solution method. First of all, it is assumed that the distribution of upstream flow velocity is known as function of r. Figure 4-11 shows a sample flow configuration on an underwater vehicle tail cone where the upstream location in this case is identified by station 1 (I = 1). The upstream flow velocity can either be uniform or nonuniform*. Station 1 is then divided into a finite number of control points including the hub and the inside wall of the shroud. In Figure 4-11, a total of 6 control points (J = 6) are used. By using the mass conservation equation (4.2.1-22), the local mass flow rate ($g_{J,J+1}$) between each two adjacent control points J and J+1 is calculated. The total mass flow rate, $\dot{G}_1$, is just the summation of local flow rates

*Note) However, the upstream flow, which is severely retarded or highly nonuniform due to, e.g., the viscous effect, may present problems of accuracy, which will be discussed in Section 4.2.3.

$$\dot{G}_1 = \sum \dot{g}_{1,J,J+1} \qquad (4.2.2\text{-}1)$$

$$\text{where } \dot{g}_{1,J,J+1} = 2\pi \int_{r_J}^{r_{J+1}} K_b \cdot \rho r \, u_{m_1}(r) \cos\phi_q \, dr \qquad (4.2.2\text{-}2)$$

For Stations I = 2,3,4..., the initial control points and initial u_m velocity profile are also needed for the iteration procedure. For the case of handling a uniform upstream flow velocity, the selection of control points, J = 1 ~ 6, and determination of initial flow velocity may be done in the same manner as that for the first Station, I = 1, since the constant velocity distribution can be assumed. However, the case of nonuniform flow velocity distribution will require a little care for selection of control points and determination of initial flow velocity distribution. Among many possible ways, it has been decided herein that the velocity distribution is assumed to have a similarity nature as that of the upstream at I = 1, i.e.,

$$u_{mI}(r) = k_I u_{m1}(r)$$

$$r = r_{H1} + \frac{r - r_{HI}}{r_{SI} - r_{HI}} \cdot (r_{S1} - r_{H1})$$

$$; \; I = 2,3.... \qquad (4.2.2\text{-}3)$$

where

r_{S1}, r_{SI} = radius of shroud internal wall at Station 1 and I ($\geq$ 2), respectively

r_{H1}, r_{HI} = radius of hub at Station 1 and I ($\geq$ 2), respectively

k_I = an arbitrary constant, dependent of Station I, to be determined later.

An arbitrary constant k_I is used to adjust the total flow rate at Station I $\geq$ 2 becomes $\dot{G}_1$ when $u_{mI}(r)$ is substituted into Eqn. (4.2.1-22). Once k_I is properly determined, the control points J = 2,3... can be determined by using Eqn.

(4.2.2-2). In order to carry out the above computations, ϕ should be known in advance. If the control points at every control station are known, ϕ can be calculated by connecting these points for each streamline by using, e.g., cubic spline method. However, at the first iteration, even these points are not yet known. Therefore, ϕ should be determined by guess. One possible way is to linearly interpolate ϕ for $2 \leq J \leq 5$ from ϕ at $J = 1$ and ϕ at $J = 6$, i.e., the hub wall angle and shroud internal wall angle, respectively.

It is now ready to calculate a new set of u_m's or $\partial u_m/\partial r$ at $I = 2,3,4...$ by using Eqn. (4.2.1-18). Since actual calculations are made on $\partial u_m/\partial r$, an integration constant should be determined to uniquely determine u_m itself. This constant can be readily determined by applying the mass conservation equation (4.2.1-22), the control points ($J = 2,3...$) at each $I \geq 2$ should be shifted according to Eqn. (4.2.2-2). Integral limits, r_J's, which determine the control points on the q-line for $J = 2,3...$ are determined one by one starting from the hub in such a way that the mass flow rate $\dot{g}_{1,J,J+1}$ remains the same in each stream sheet as that for $I = 1$. This iteration process must be repeated until convergence for u_m's as well as the location of control points (or streamlines) is obtained.

4.2.3 Potential Problems of SCM for Highly Nonuniform Velocity Profile Due to Viscosity

The present streamline curvature method (SCM) to be used for determining the meridional flow streamlines is based on the momentum equation and mass conservation equation with viscous effects totally ignored. Therefore, if the upstream flow is the one fully retarded due to the viscous effect, i.e., boundary layer flow, so that the velocity distribution is highly nonlinear, the application of the present SCM may create substantial inaccuracy in determining the location and velocity of streamlines. This point is clearly understood by investigating the momentum equation

(4.2.1-19); P(r) and T(r) are only dependent upon r except for r_m which is a function of curvature of streamline. It means that u_m is a weak function of the axial-direction coordinate so that u_m at a certain station is almost entirely determined by the inner and outer wall curvature. No matter how strongly the incoming flow velocity is retarded, the flow velocity will become more or less uniform before the flow travels too far downstream because the curvature effect (r_m) cannot last too long.

The above discussions seem to suggest that the development of streamline curvature method (SCM) with viscous effect incorporated may be in order, particularly for handling the highly viscous flow near the tail cone area of underwater vehicle.

The momentum equation for such a flow should be of the form

$$\underline{u} \times \underline{\omega} = \nabla H - T\nabla S - \nu\nabla^2\underline{u} \qquad (4.2.3\text{-}1)$$

instead of Eqn. (4.2.1-8).

One additional term will make the problem extremely complex and this problem will be handled in the FY-86 GHR program.

4.2.4 Numerical Results

The streamline curvature method described in Sections 4.2.1 and 4.2.2 was used to calculate the streamlines for a typical underwater vehicle tail cone area with a shroud. In the present case the upstream flow velocity was assumed to be uniform. A total of 14 q-lines (I = 14) were used with 5 control points (J = 5) at each q-line, see Figure 4-12. The solid lines are the initial guess for the streamlines whereas the dashed lines are the converged solution for the final streamlines. It is seen from this figure that these two sets of lines match well to each other except for the area behind the middle chord of rotor. It means that the initial guess used here was very accurate until the flow

passes the rotor and stator. Due to the initial accurate guess for streamlines, computer time was minimal.

4.3 BLADE-TO-BLADE FLOW

4.3.1 Transformation

Under the assumption that an axisymmetric stream surface exists in a rotating machine, from the conservation equation of circulation, i.e, $\underline{\nabla} \times \underline{w} + 2\underline{\omega} = 0$, the following relation is obtained for the relative flow,

$$\frac{\partial w_m}{\partial \theta} - \frac{\partial (r w_\theta)}{\partial m} = 2\omega r \frac{\partial r}{\partial m} \qquad (4.3.1\text{-}1)$$

where w_m and w_θ are relative flow velocities in the direction of m and θ, see Figure 4-13. The continuity equation for the same stream surface is also written

$$\frac{\partial (b\rho w_\theta)}{\partial \theta} + \frac{\partial (b\rho r w_m)}{\partial m} = 0 \qquad (4.3.1\text{-}2)$$

where b is the thickness of stream surface.

Then, a stream function Ψ can be defined as

$$w_\theta = \frac{1}{b\rho} \frac{\partial \Psi}{\partial m} \ , \ w_m = - \frac{1}{b\rho} \frac{\partial \Psi}{r \partial \theta} \qquad (4.3.1\text{-}3)$$

Substitution of w_θ and w_m in Eqn. (4.3.1-3) into Eqn. (4.3.1-1) yields

$$\frac{\partial^2 \Psi}{r^2 \partial \theta^2} + \frac{\partial^2 \Psi}{\partial m^2} + \left(\frac{1}{r} \frac{\partial r}{\partial m} - \frac{1}{b} \frac{\partial b}{\partial m} \right) \frac{\partial \Psi}{\partial m} = -2b\rho\omega \sin\lambda \qquad (4.3.1\text{-}4)$$

where λ is the angle of the line tangent to the stream surface at the point of interest made with the axis of rotation, see Figure 4-13.

This three-dimensional axiymmetric stream surface can be mapped onto a two-dimensional plane, (X, Y), see Figure 4-14, by the following mapping functions

$$\frac{dX}{dm} = \frac{r_o}{r} \ , \ \frac{dY}{d\theta} = -r_o \ , \qquad (4.3.1\text{-}5)$$

where r_o is an arbitrary constant which is used for the purpose of scaling between the physical coordinate space and mapped plane, (X, Y). The governing equation (4.3.1-4) can now be written in the (X, Y) coordinate system by using Eqn. (4.3.1-5)

$$\nabla^2\psi = -2b\rho\omega \left(\frac{r}{r_o}\right)^2 \sin\lambda + \frac{1}{b\rho}\left\{\frac{\partial(b\rho)}{\partial X}\frac{\partial\psi}{\partial X} + \frac{\partial(b\rho)}{\partial Y}\frac{\partial\psi}{\partial Y}\right\}. \qquad (4.3.1\text{-}6)$$

Also, the relative velocities in the X- and Y-directions are given

$$\text{(a)} \ w_X = \frac{1}{b\rho}\frac{\partial\psi}{\partial X} = \frac{r}{r_o} w_m$$

$$\text{(b)} \ w_Y = -\frac{1}{b\rho}\frac{\partial\psi}{\partial Y} = -\frac{r}{r_o} w_\theta. \qquad (4.3.1\text{-}7)$$

As seen from Eqn. 4.3.1-6, the governing equation for the (X, Y) plane is now a Poisson equation instead of the Laplace equation, which exists only for a flow on a perfectly cylindrical stream surface. Therefore, the results obtained from the two-dimensional linear cacade theory should be corrected according to the right-hand side term of Eqn. (4.3.1-6). It is readily understood that these right-hand side terms are satisfied by distributing the following vortices and sources on the entire (X, Y) plane

$$\text{(a)} \ \zeta = (\nabla \times \underline{w})_{X,Y} = 2\omega \left(\frac{r}{r_o}\right)^2 \sin\lambda$$

$$\text{(b)} \ \mu = (\nabla\cdot\underline{w})_{X,Y} = -\frac{1}{(b\rho)^2}\left\{\frac{\partial(b\rho)}{\partial X}\frac{\partial\psi}{\partial Y} - \frac{\partial(b\rho)}{\partial Y}\frac{\partial\psi}{\partial X}\right\}. \qquad (4.3.1\text{-}8)$$

By adding the induced velocities calculated from ζ and μ, the blade profile shape or equivalently the camber obtained

in the conventional two-dimensional analysis will be corrected. It should be noted that the first term on the right-hand side of Eqn. (4.3.1-6) arises from non-zero λ, i.e., the stream surface is not parallel to the axis of rotation, whereas the second group of terms is due to the non-uniform thickness of stream surface or tube. Needless to say, if $\lambda = 0$ and b_p is constant, Eqn. (4.3.1-6) becomes a Laplace equation and thus a two-dimensional linear cascade theory holds.

A method similar to the present one was developed by Inoue and his colleague (e.g., the paper by Inoue, et al. (1980)). In this paper there exist a few major drawbacks, some of which could potentially lead to a substantial error in the final design. First of all, since they use a two-dimensional linearized cascade theory, the error becomes significant for high solidity and high stagger angle area, i.e., near the hub, although they introduce experimental data in a later step of the analysis. Secondly, their velocity triangle used for determining the incoming flow angle to the blade is in error of the first order since they did not take into consideration the effect of non-cylindrical and variable thickness stream surface. Finally, due to the use of the linearized cascade theory, they failed to obtain the velocity distribution so that a boundary layer analysis and cavitation inception analysis are not possible.

With these aspects in mind, effort has been made in the current GHR project to improve the accuracy of the linear cascade theory as well as to avoid the singular behavior of velocity at the leading edge of blade, see Section 4.3.2 and Section 4.3.3, respectively. The detailed analysis and numerical procedure for the vorticity and source corrections on the two-dimensional flow are yet to be developed and will be handled in the FY-86 GHR program.

4.3.2 Loading Correction on Linearized Cascade Theory

The cascade lift coefficients calculated based on linearized theory are found unsatisfactory. Two correction factors are proposed in the present study to determine the effective lift coefficient which fit better to the experimental data.

According to the linearized cascade theory (Mellor, 1959), the ideal theoretical lift coefficient can be obtained as a function of the mean angle of attack, α_m, camber distribution, $y_c(x)$; blade thickness distribution, $y_t(x)$; solidity, σ; and stagger angle, λ. The results are compared with the NACA 65-series experimental data given by Herrig, et al. (1951).

The correlation between the calculated and measured lift coefficients is depicted in Figure 4-15. With β_1 denoting the upstream flow angle relative to the cascade axis, the results for a sample case of $\beta_1 = 45°$ and $\sigma = 1.5$, with NACA 65-(15)10, are shown in Figure 4-16. These figures indicate that the calculated results obtained from the linearized theory are in general higher than the laboratory data.

Mellor (1959) did a similar comparison study and found that the effects due to the camber-line slopes at the blades extremities may be suppressed to yield results closer to the laboratory data. Under this concept of reducing the camber effect, he suggested to take

$$C_{b(effective)} = 0.725\ C_{b(theoretical)} \qquad (4.3.2\text{-}1)$$

when C_b denotes the single-foil camber. The effective C_b is the one to be used in the model to find an effective lift coefficient suitable for any application.

The generated lift coefficients calculated following his suggestion are compared to the measured values and shown in Figures 4-17 and 4-18. The results are improved when com-

pared to Figures 4-15 and 4-16 which are obtained from the case without applying any modification factor.

After following Mellor's suggestion of C_b modification, although the deviation between the theoretical result and laboratory data is reduced, the obvious difference still exists, especially at a high flow angle. In order to further reduce the deviation, the present study employs dual modification factors K_{Cb} and K_α such that

$$C_{b(eff.)} = K_{Cb}\, C_{b(theor.)} \qquad (4.3.2\text{-}2)$$

and

$$\alpha_{m(eff.)} = K_{\alpha m}\, \alpha_{m(theor.)} \qquad (4.3.2\text{-}3)$$

These two factors are determined by having the least deviation between the calculated lift coefficient and the corresponding measured values. The details are described in the following.

For a combination of K_{Cb} and $K_{\alpha m}$, a set of C_{L_1} as a function of C_b, σ, β_1, and α_1 is calculated from the linearized model. For each trial combination of K_{Cb} and $K_{\alpha m}$, the computed C_{L_1} is compared to the measured values and a value of the standard deviation is produced. The set of K_{Cb} and $K_{\alpha m}$ which gives minimum standard deviation is taken as the desired coefficients to produce the best fitted results.

The application of $K_{\alpha m}$ in addition to K_{Cb} yields further reduction of the error. If the results are examined with the coefficients read at an interval of 0.05, the minimum standard deviation of the residuals for all data occurs at $(K_{Cb}, K_{\alpha m}) = (0.7, 0.75)$. If the available data is divided into four groups of $\beta_1 = 30°$, $45°$, $60°$, and $70°$, the minima occur at (0.75, 0.8), (0.65, 0.85), (0.65, 0.7), and (0.6, 0.75), respectively. If examined at an interval of 0.01, these five sets of results are (0.69, 0.74), (0.73, 0.83), (0.67, 0.79), (0.63, 0.73), and (0.62, 0.71), respectively.

The correlation between the model results and laboratory results is given in Figure 4-19. The improvements of applying the modification factors can be found by comparing these figures to Figures 4-15 and 4-17. Without using the factors (Figure 4-15), the model overpredicts the results in general, with the higher residual for higher lift coefficient which is associated with higher angle of incidence. After applying K_{Cb} = 0.725 as suggested by Mellor (1959), the standard deviation of the residuals decreases from 0.118 in Figure 4-15 to 0.060 in Figure 4-17. With a combination of (K_{Cb}, $K_{\alpha m}$) = (0.7, 0.75), the resultant value fits much better to the measured value (Figure 4-19) and the standard deviation becomes only 0.026.

With only K_{Cb} = 0.725, a sample comparison of the calculated and measured lift coefficient (Figure 4-18) shows an improvement from that in Figure 4-16. Yet the results are still too high and are worse at higher angle of attack. With (K_{Cb}, $K_{\alpha m}$) = (0.7, 0.75), the result is much better, as shown in Figure 4-20. The residuals are now more or less evenly distributed over the angle of attack (and over the magnitude of lift coefficient).

This study of loading correction on linearized cascade theory is conducted to provide realistic loading data. Both the single-foil camber, C_b, and angle of attack, α_m, are multiplied by discount factors before they are used in the theoretical model to calculate the cascade lift coefficient. The discount factors are determined based on a set of laboratory data. This engineering approach of obtaining the desired lift coefficient is deemed appropriate to provide data to be used in a propulsor blade design procedure.

In the linearized cascade theory (Mellor, 1959), it is assumed that the difference between the induced velocity on the blade surface and on the camber line is negligible. This assumption is not valid under certain circumstances.

The errors are proportional to the square of camber and square of relative thickness as indicated by Mellor (1959). Thus it is planned to take a theoretical approach in the future study, instead of the present engineering approach, to correct the errors due to assumptions adopted in the linearized theory. The singularities are to be distributed on the camber line or even on the blade surfaces instead of on the chord line. In this way, the results will be more accurate by paying for extra complicity in the solution procedure.

4.3.3 Leading Edge Correction on Linearized Cascade Theory

The second disadvantage of using the linearized cascade theory stems from the fact that a singularity in terms of flow velocity exists at the blade leading edge. This singularity is integrable so that it will present no problem of calculating the force on the blade. It will, however, cause inconvenience whenever a detailed velocity distribution is required, e.g., for calculation of viscous boundary layer or cavitation inception on the blade.

The objective of the study in this Section is therefore to correct such problem and then to provide an accurate velocity distribution. The method employed here is a singular perturbation method widely used in fluid flow problems, see e.g., a textbook by Van Dyke (1975), a paper by Furuya and Acosta (1973). The method is particularly useful for a case in which a solution is regular everywhere except for a localized singularity.

The velocity obtained from a linearized cascade theory (see Mellor (1959)) is given

$$\frac{q}{q_m} = 1 \pm 2\pi A_0 \cdot \Gamma_{00} \pm 2\pi A_1 \cdot \Gamma_{01} \pm 2 \sum_{n=2}^{\infty} A_n \sin n\theta + F(\theta(x)) \qquad (4.3.3\text{-}1a)$$

$$F(\theta(x)) = \left[-\frac{c}{s} \int_0^1 \gamma(\theta_0) \cdot I(\theta,\theta_0)\, d\left(\frac{x_0}{c}\right) \right.$$

$$+ \frac{1}{2} \int_0^1 \frac{t}{c} f_t'(\theta_0) \frac{d\left(\frac{x_0}{c}\right)}{(x-x_0)/c}$$

$$\left. + \frac{c/s}{2} \int_0^1 \frac{t}{c} f_t'(\theta_0)\, R(\theta,\theta_0)\, d\left(\frac{x_0}{c}\right) \right] \sqrt{1+y_c'^2}$$

(4.3.3-1b)

where $\pm$ corresponds to the upper and lower side of the blade,

$$\frac{\gamma}{q_m} = 2A_0 \frac{1+\cos\theta}{\sin\theta} + 4 \sum_{n=1}^{\infty} A_n \sin n\theta,$$

q_m = geometric mean velocity of upstream and downstream velocities, q_1 and q_2,

$\cos\theta = 1-2\,x/c$,

$\cos\theta_0 = 1-2\,x_0/c$, where θ_0, x_0 are used as dummy variables,

c = chord length,

$y_c = C_b \cdot f_c(\frac{x}{c})$ (= camber function),

$$R(\theta,\theta_0) = \frac{1}{\pi}\left[\sum_{1}^{\infty} + \sum_{-\infty}^{-1}\right] \frac{\frac{x-x_0}{c}\frac{c}{s} - n\sin\lambda}{\left(\frac{x-x_0}{c}\frac{c}{s} - n\sin\lambda\right)^2 + n^2\cos^2\lambda},$$

$$I(\theta,\theta_0) = \frac{1}{\pi}\left[\sum_{1}^{\infty} + \sum_{-\infty}^{-1}\right] \frac{n\cos x}{\left(\frac{x-x_0}{c}\frac{c}{s} - n\sin\lambda\right)^2 + n^2\cos^2\lambda},$$

s = cascade blade spacing,

λ = stagger angle of cascade,

$y_t = t \cdot f_t(\frac{x}{c})$ (= thickness distribution function),

$$\Gamma_{00} = \frac{1+\cos\theta}{2\pi\sin\theta} \quad \text{and} \ ,$$

$$\Gamma_{01} = \frac{\sin\theta}{\pi} \ .$$

As clearly seen from Γ_{00} term, the velocity becomes singular at the leading edge, i.e., as $x \to 0$ (i.e., $\theta \to 0$). The lift coefficient C_ℓ can be calculated based on this velocity

$$C_\ell = \frac{p_\ell - p_u}{\frac{1}{2}\rho q_m^2} = \int_0^1 \left[\left(\frac{q_u}{q_m}\right)^2 - \left(\frac{q_\ell}{q_m}\right)^2\right] d\left(\frac{x}{c}\right)$$

$$= 2\pi A_0 + 2\pi A_1. \qquad (4.3.3\text{-}2)$$

It is noted that, although the velocity has a singularity at the leading edge, the velocity squared is integrable so that the force can be conveniently calculated. It should also be mentioned that only the first two circulation terms, i.e., Γ_{00}, Γ_{01}, remain for the lift calculation. By expanding the leading edge area of $y = \pm \varepsilon\sqrt{x}$ with $x = \varepsilon^2 X$ and $y = \varepsilon^2 Y$ where the leading edge radius $R = \varepsilon^2/2$, the flow velocity becomes (see the paper of Furuya (1983)),

$$q_i = U_i \sqrt{\frac{X}{X+1/4}} \left| 1 \pm \frac{a}{\sqrt{X}} \right| \qquad (4.3.3\text{-}3)$$

where $X=a^2$ denotes the X-coordinate of stagnation point and U_i is the flow velocity at upstream infinity in the inner region. The inner region is represented by (X,Y) which is stretched by the scale of ε^2. Also, in the present method, it is assumed that the round leading edge profile of any blade can be accurately approximated by a parabola. Rewriting Eqn. (4.3.3-3) in terms of x and expanding it as $x \to \infty$,

$$q_i = U_i \sqrt{\frac{1}{1+\varepsilon^2/4x}} \left| 1 \pm \frac{\varepsilon a}{x^{1/2}} \right|$$

$$= U_i \left(1 \pm \frac{\varepsilon a}{x^{1/2}} + O(\varepsilon^2)\right). \qquad (4.3.3\text{-}4)$$

Expansion of the outer solution in Eqn. (4.3.3-1a) as $x \to 0$ becomes, after some algebra,

$$\frac{q}{q_m} = 1 \pm \frac{A_0}{\sqrt{x}} + O(\varepsilon). \qquad (4.3.3\text{-}5)$$

Matching the inner solution (4.3.3-4) with the outer solution (4.3.3-5) yields

$$U_i = q_m$$

$$\varepsilon a = A_0 \qquad (4.3.3\text{-}6)$$

The uniformly valid solution (see the book of Van Dyke (1975)) can then be constructed

$$\frac{q_{uniform}}{q_m} = 1 \pm 2\pi A_0 \Gamma_{00}(\theta) \pm 2\pi A_1 \Gamma_{01}(\theta)$$

$$\pm 2 \sum_{n=2}^{\infty} A_n \sin n\theta + F(\theta(x))$$

$$+ \sqrt{\frac{x}{x+\varepsilon^2/4}} \left| 1 \pm \frac{A_0}{x^{1/2}} \right| - \left(1 \pm \frac{A_0}{x^{1/2}} \right) \qquad (4.3.3\text{-}7)$$

where $F(\theta(x))$ is defined in Eqn. (4.3.3-1b). It should be noted that the uniformly valid solution no longer has a singularity since the second term together with the last term in Eqn. (4.3.3-7) now has a finite value as $x \to 0$.

The above results were used to compare the analytically predicted velocity profile with experimental data. Four different such results using NACA 65-series airfoil are shown in Figure 4-21. Not only the singular behavior which would exist with the linearized cascade theory has disappeared but also the agreement is good enough to be applicable for boundary layer and cavitation inception analyses.

5.0 CONCLUSIONS

Through the FY-85 GHR program, the following major subjects have been investigated:

- o It has been concluded that among three possible candidate design theories which can incorporate three-dimensionality into pumpjet design procedure, the blade-through flow with blade-to-blade flow method has been selected as the appropriate design method for the present study.

- o The selected design method is of an iterative type, which includes the following sub-theories:

  (a) the determination of the shroud intake diameter,

  (b) the determination of the streamline by a streamline curvature method (SCM),

  (c) mapping of the stream surface calculated through the SCM onto a plane hence producing a Poisson equation due to the cone shaped stream surface,

  (d) modifying the blade profile shape obtained in the potential theory through a method of correcting the effect of the Poisson equation on the potential theory results,

  (e) improving the prediction accuracy of the two-dimensional cascade theory by using a pair of correction factors such that the loadings calculated through the linearized cascade theory fit well with the experimental data.

  (f) removing the singularity at the leading edge of the two-dimensional cascade theory by applying the singular perturbation method so that a useful velocity profile can be obtained to be later used for flow separation and cavitation analyses.

  (g) checking for the possibility of flow separation, and

  (h) checking for the chance of cavitation inception.

- o Among the above sub-theories (a) - (h), the theory development of (a), (b), (e), and (f) has been accomplished during FY-85.

For the FY-86 GHR program, it is planned to perform the following:

- develop the detailed theoretical formula for the diagonal flow, (c) and (d) above,

- develop a theoretical approach to improve the result of loading calculated through a linearized cascade theory, e.g., having singularities distributed on the camber instead of the chord line, an additional work for (e), and

- develop a foundation for a unified pumpjet design theory by incorporating all the sub-theories developed above.

6.0 REFERENCES

Bruce, E.P., Gearhart, W.S., Ross, J.R., and Treaster, A.L., 1974, "The design of pumpjets for hydrodynamic propulsion," Fluid Mechanics, Acoustics, and Design of Turbomachinery, Part I, NASA SP-304, 795-839.

Crocco, L., 1937, Z. angew. Math. Mech., 17, 1.

Furuya, O., and Acosta, A.J., 1973, "A note on the calculation of supercavitating hydrofoils with rounded noses," Journal of Fluids Eng., ASME, 95, 221-228.

Furuya, O., Chiang, W.-L., and Maekawa, S., 1984, "A hydrodynamic study of the ALWT (MK-50) pumpjet," Tetra Tech Report TC-3725, Tetra Tech, Inc., Pasadena, CA.

Herrig, L.J., Emery, J.C., and Erwin, J.R., 1951, "Systematic two-dimensional cascade tests of NACA 65-series compressor blade at low speeds", NACA RM L51G31, National Advisory Committee for Aeronautics, Washington, D.C.

Inoue, M., Ikui, T., Kamada, Y., and Tashiro, M., 1980, "A quasi three-dimensional design of diagonal flow impellers by use of cascade data," IAHR Symposium 1980, Tokyo, 403-414.

Katsanis, T., 1964, "Use of arbitrary quasi-orthogonals for calculating flow distribution in the meridional plane of a turbomachine," NASA TN D-2546, National Aeronautics and Space Administration, Washington, D.C.

Kerwin, J.E., and Leopold, R., 1964, "A design theory for subcavitating propellers, Trans. SNAME, 72.

Mellor, G.L., 1959, "An analysis of axial compressor cascade aerodynamics; Part I, Potential flow analysis with complete solutions for symmetrically cambered airfoil families; Part II, Comparison of potential flow results with experimental data", Journal of Basic Engineering, 81, 362-378 and 379-386.

Van Dyke, M., 1975, Perturbation Methods in Fluid Mechanics, Annotated edition, The Parobolic Press, Stanford, CA.

APPENDIX

CALCULATION OF HEAD LOSS COEFFICIENT K_1
(Between Reference Point ① and Rotor Inlet ②)

The energy loss between ① and ② can be given

$$\Delta E = \left[\text{Head} \cdot d\dot{m}\right]_{①}^{②} = \left[\int \frac{p_s + \rho\frac{v^2}{2}}{\rho g}\, d\dot{m}\right]_{①}^{②}$$

$$= \int_{r_{H1}}^{r_{T1}} \left(\frac{p_{s1}}{\rho g} + \frac{V_1^2}{2g}\right) 2\pi r V_1 dr \cos\theta_1$$

$$- \int_{r_{H2}}^{r_{T2}} \left(\frac{p_{s2}}{\rho g} + \frac{V_2^2}{2g}\right) 2\pi r V_2 dr \frac{1}{\cos\theta_2} \qquad (1)$$

$$\Delta H = \frac{\Delta E}{\text{Total Mass Flow Rate}}$$

$$= \frac{\int_{r_{H1}}^{r_{T1}} \left(\frac{p_{s1}}{\rho g} + \frac{V_1^2}{2g}\right) 2\pi r V_1 \cos\theta_1\, dr}{\int_{r_{H1}}^{r_{T1}} V_1 2\pi r \cos\theta_1\, dr}$$

$$- \frac{\int_{r_{H2}}^{r_{T2}} \left(\frac{p_{s2}}{\rho g} + \frac{V_2^2}{2g}\right) 2\pi r V_2 \frac{1}{\cos\theta_2} \cdot dr}{\int_{r_{H2}}^{r_{T2}} V_2 2\pi r \frac{1}{\cos\theta_2}\, dr} \qquad (2)$$

Defining $p_t = p_s + \frac{1}{2}\rho V^2$ (total pressure), (3)

$$C_{Pt} = \frac{p_T - p_\infty}{\frac{1}{2}\rho V_\infty^2} \quad \text{(total pressure coefficient)}, \tag{4}$$

and $$C_{Ps} = \frac{p_s - p_\infty}{\frac{1}{2}\rho V_\infty^2} \quad \text{(static pressure coefficient)} \tag{5}$$

$$\frac{\Delta H}{V_\infty^2/2g} = \frac{1}{V_\infty^2/2g \int_{r_{H1}}^{r_{T1}} V_1 r \cos\theta_1 \, dr}$$

$$\left[\int_{r_{H1}}^{r_{T1}} \frac{1}{\rho g} \left(C_{Pt_1} \frac{1}{2}\rho V_\infty^2 + p_\infty\right) r V_1 \cos\theta_1 \, dr \right.$$

$$\left. - \int_{r_{H2}}^{r_{T2}} \frac{1}{\rho g} \left(C_{Ps_2} \frac{1}{2}\rho V_\infty^2 + P_\infty + \frac{1}{2}\rho V_2^2\right) \frac{1}{\cos\theta_2} r V_2 \, dr \right]$$

$$= \frac{}{\int_{r_{H1}}^{r_{T1}} V_1 r \cos\theta_1 \, dr} \left[\int_{r_{H1}}^{r_{T1}} \left(C_{Pt_1} r V_1 \cos\theta_1 \, dr \right.\right.$$

$$\left.\left. - \int_{r_{H2}}^{r_{T2}} \left[C_{Ps_2} + \left(\frac{V_2}{V_\infty}\right)^2\right] r V_2 \frac{1}{\cos\theta_2} \, dr \right]\right.$$

$$= \frac{1}{\int_{r_{H1}/r_B}^{r_{T1}/r_B} \left(\frac{V_1}{V_\infty}\right) \frac{r}{r_B} \cos\theta_1 \, d\left(\frac{r}{r_B}\right)}$$

$$\left[\int_{r_{H1}/r_B}^{r_{T1}/r_B} C_{Pt1} \frac{r}{r_B} \frac{V_1}{V_\infty} \cos\theta_1 d\left(\frac{r}{r_B}\right) \right.$$

$$- \int_{r_{H2}/r_B}^{r_{T2}/r_B} \left[C_{Ps_2} + \left(\frac{V_2}{V_\infty}\right)^2 \right] \frac{r}{r_B} \frac{V_1}{V_\infty} \frac{1}{\cos\theta_2} d\left(\frac{r}{r_B}\right) \Bigg] \quad (6)$$

Since C_{Pt_1}, C_{Ps_2} and V_2 are given as a function of r in the report of Treaster (1977) (see Figures 4 and 5), we can determine $\Delta H/V_\infty^2/2g$ and thus K_1 as follows

$$\frac{\Delta H}{V_\infty^2/2g} = K_1 \left(\frac{\tilde{V}_1}{V_\infty}\right)^2 \quad (7)$$

where $\Delta H/V_\infty^2/2g$, and $\frac{\tilde{V}_1}{V_\infty}$ (Eqn. (24)) are both calculated.

Table 3-1

Qualitative Comparisons for the Candidate Methods as a Three-Dimensional Pumpjet Design Method

Method / Feature	Method I Katsanis Method	Method II Blade-Through/ Blade-to-Blade Flow	Method III Singularity Distribution Method
Three-Dimensionality	O	Δ	O
Determination of Detailed Blade Profile Shape	X	O	O
Accuracy in Sectional Blade Loading	Δ	O	Δ
Calculation of Pressure/ Velocity Distribution	Δ	O	Δ
Simplicity in Numerical Computations	Δ	Δ	X
Design Capability	Δ	O	O
Overall Evaluation	Δ	O	Δ

O: Excellent
Δ: Good
X: Poor

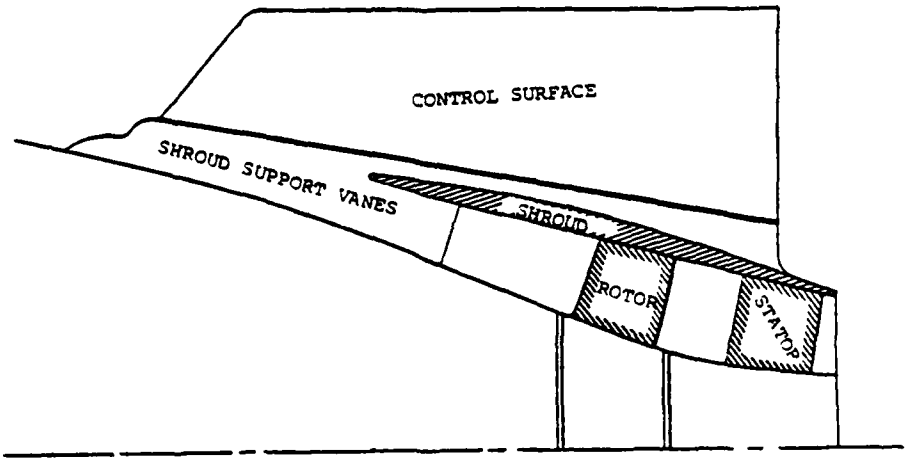

FIGURE 1-1 A typical pumpjet blade and shroud configuration

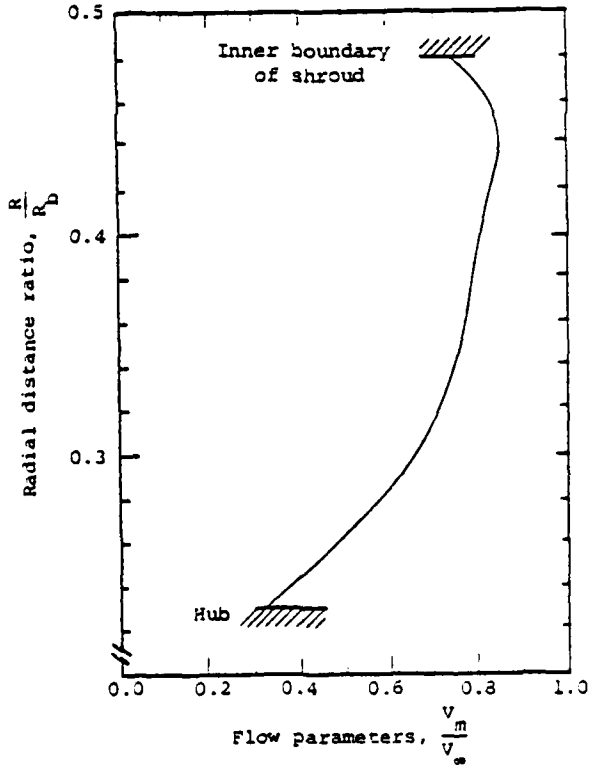

FIGURE 1-2 A typical meridional flow velocity (V_m) distribution for a pumpjet where V_∞ is upstream flow velocity

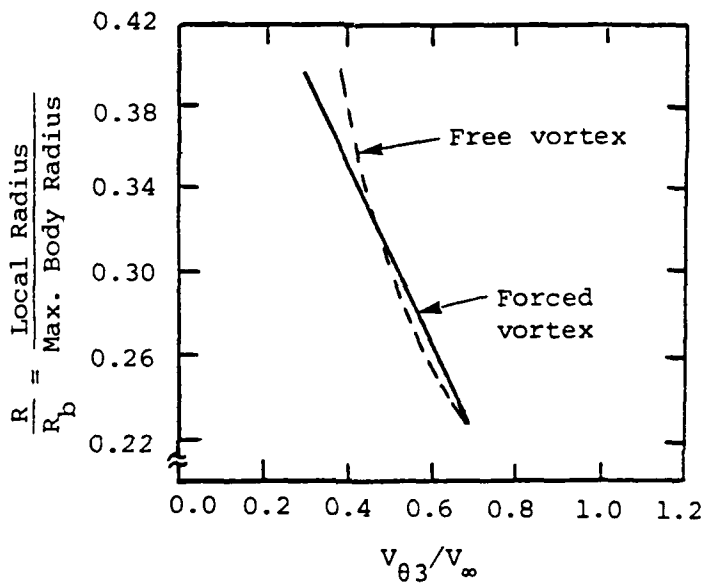

FIGURE 1-3 A typical load distribution in terms of $V_{\theta 3}$ for pumpjet rotor blade where $V_{\theta 3}$ is circumferential component of the turned flow velocity

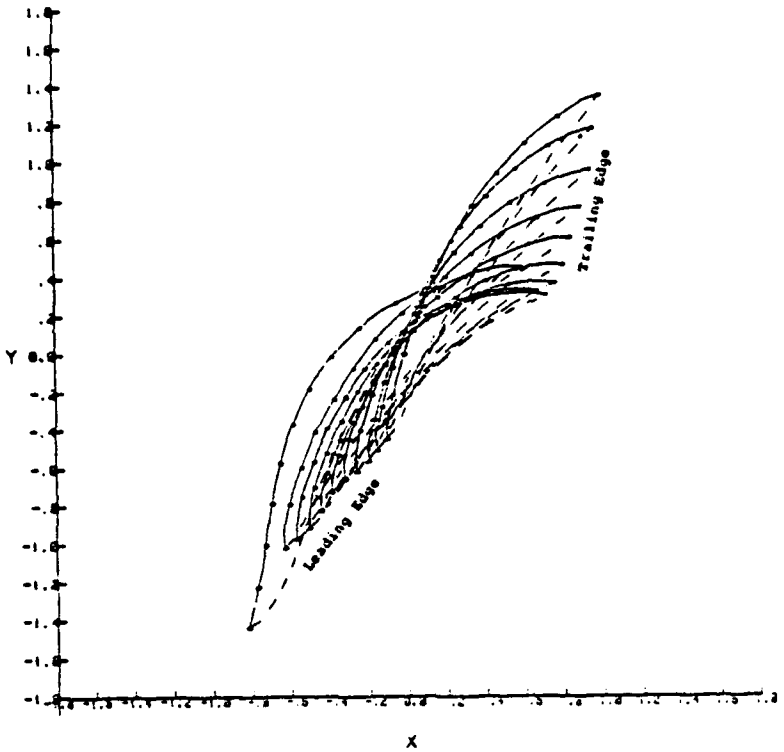

(a)

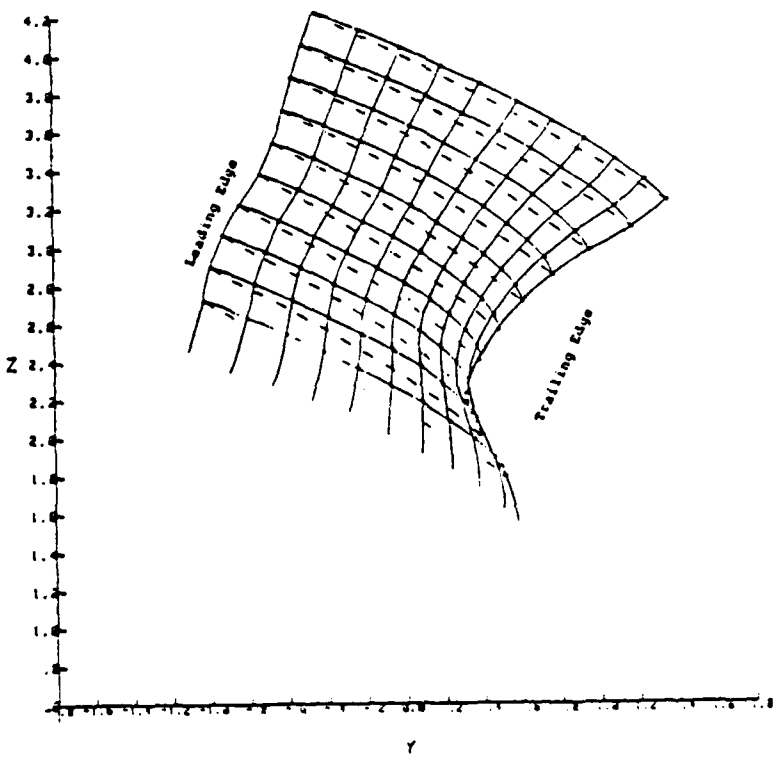

(b)

FIGURE 1-4 Typical pumpjet rotor blade configuration, (a) top view and (b) upstream view

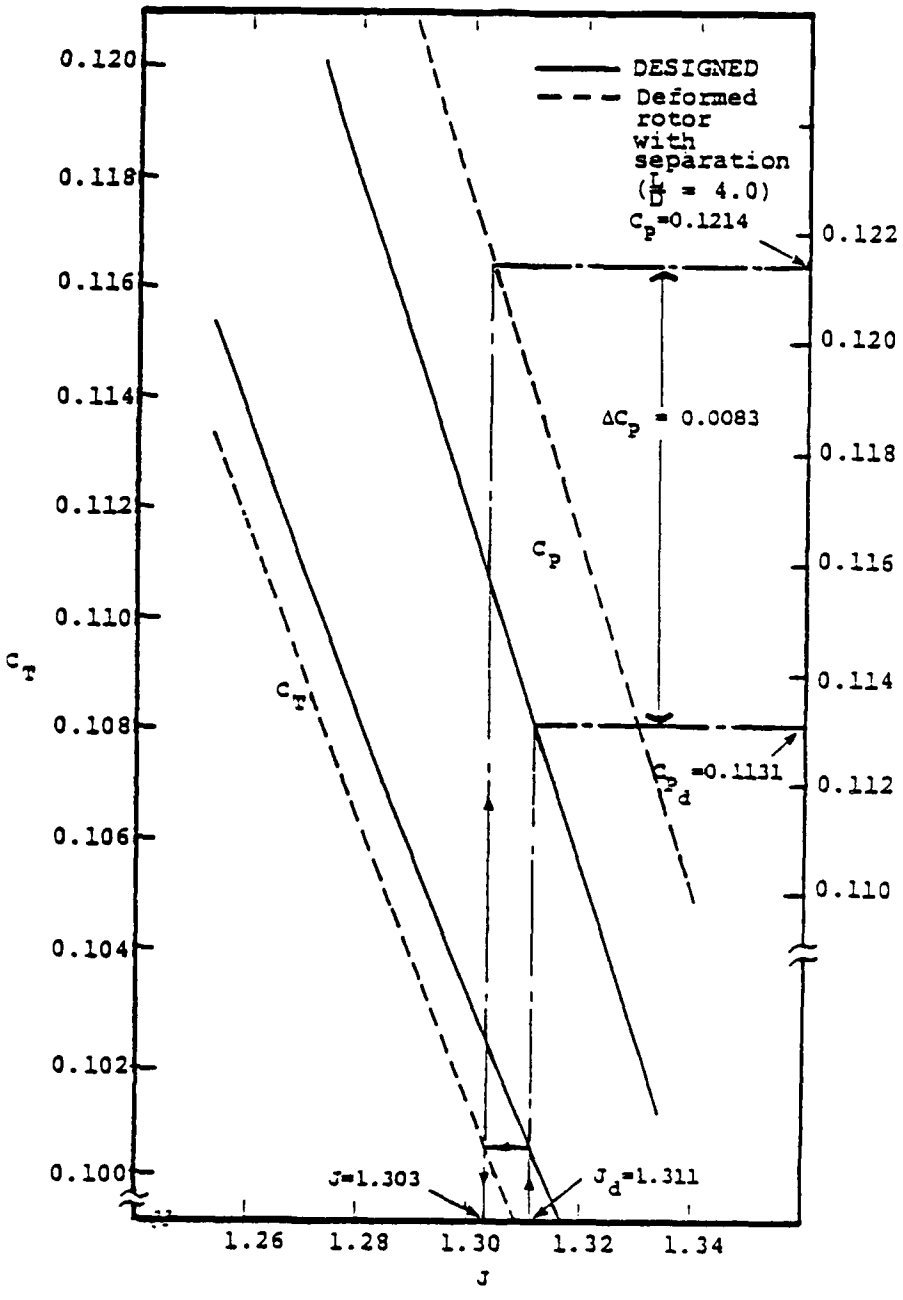

FIGURE 1-5 Typical C_P and C_T curves for the designed rotor blade profiles and deformed rotor blade profiles, showing about 7.3% increase of C_P (i.e., ΔC_P = .0083) where the design J_d = 1.311

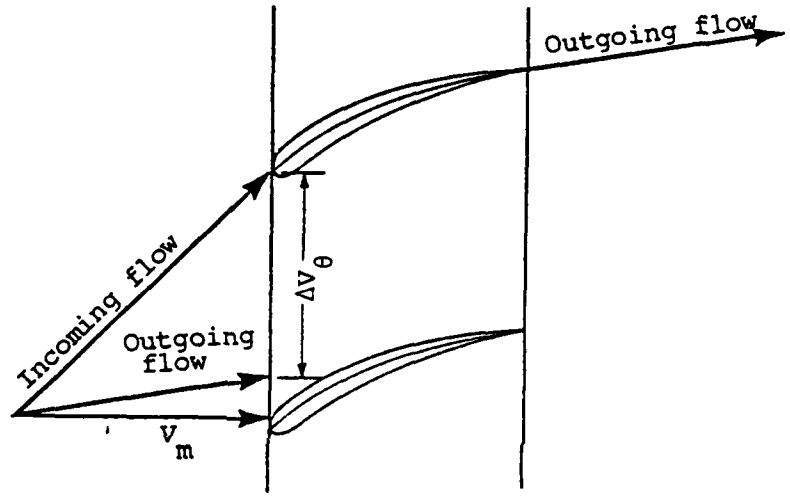

FIGURE 1-6 Flow configuration for cascade

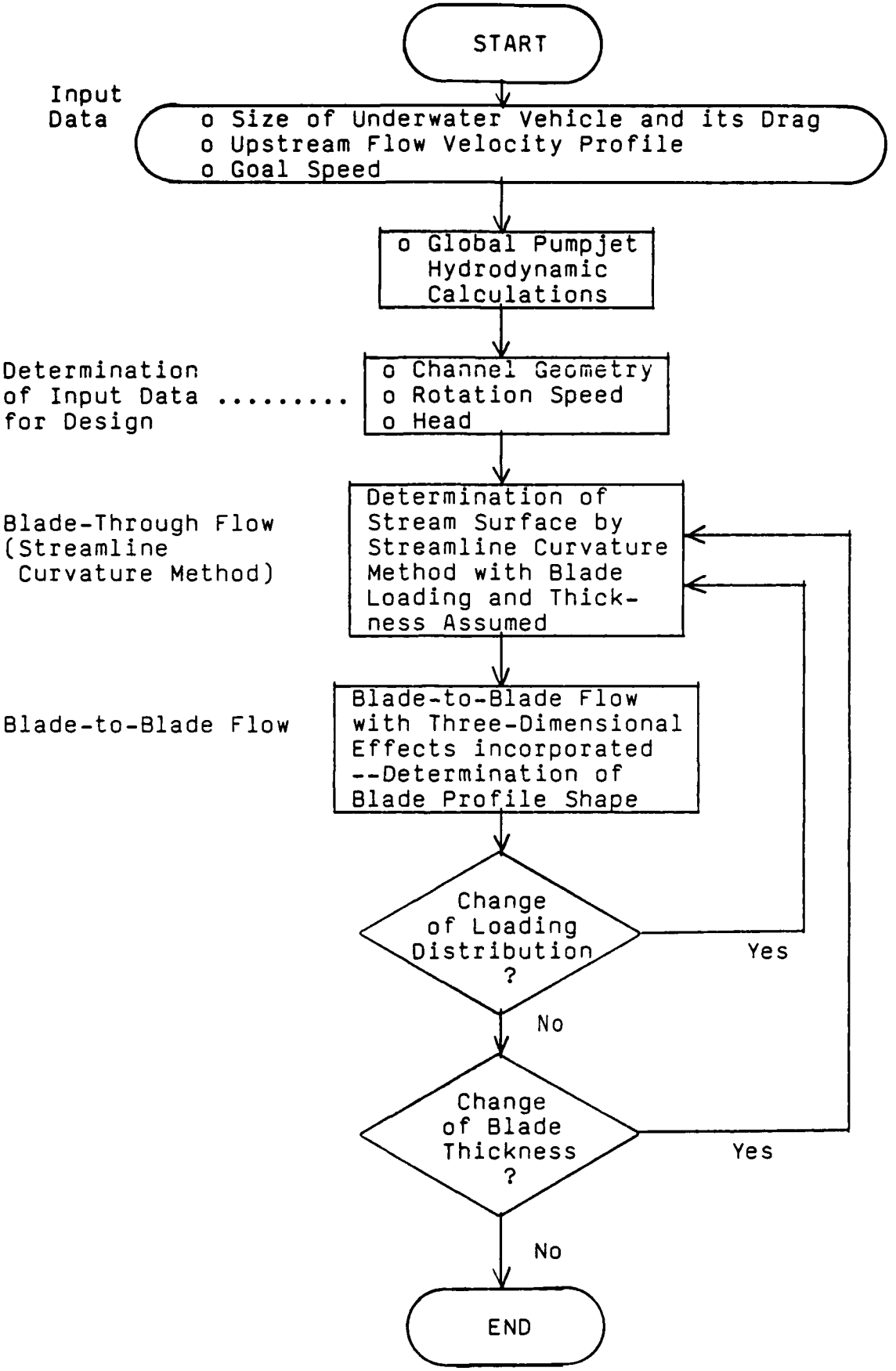

FIGURE 4-1 Flow Chart of the Selected Pumpjet Design Method

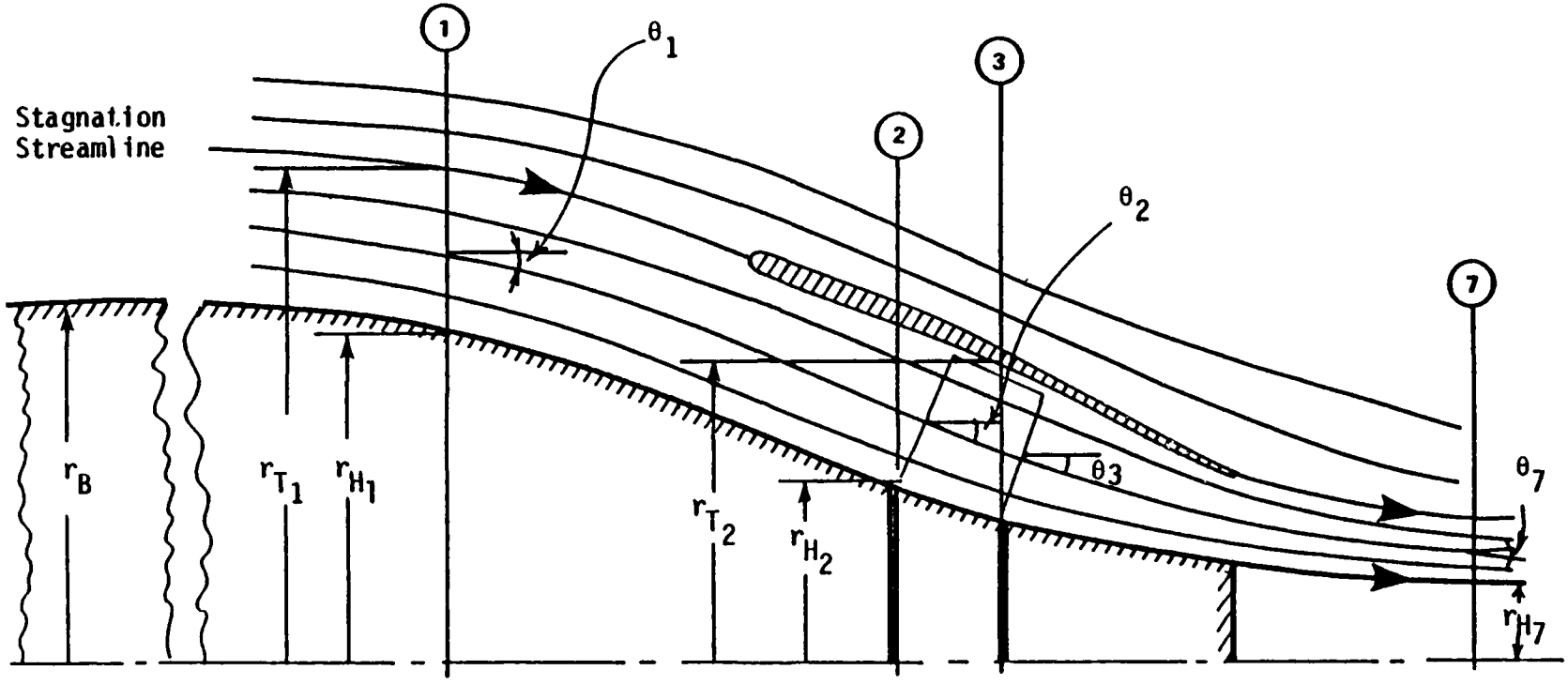

FIGURE 4-2 Schematic diagram of pumpjet flow

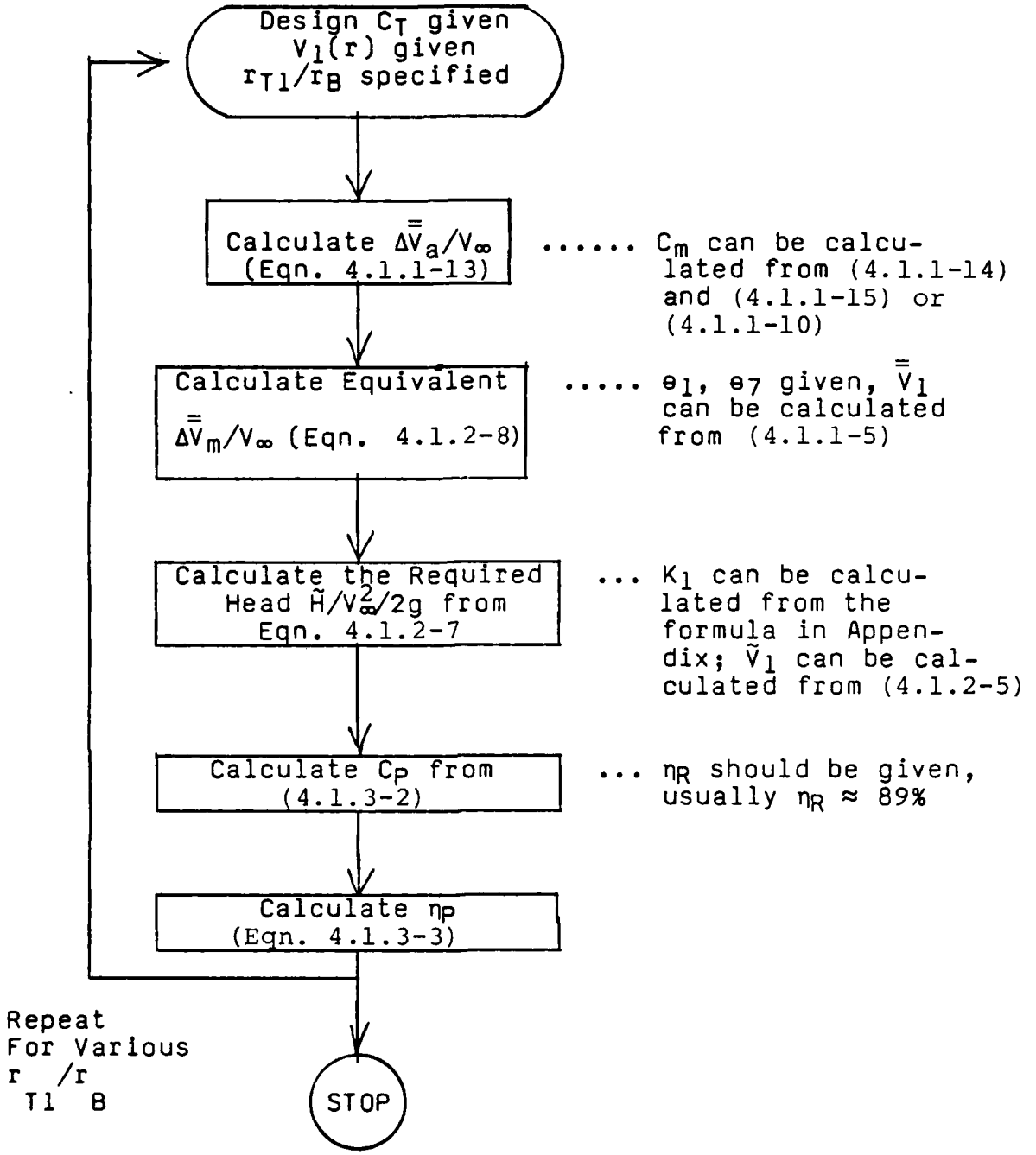

FIGURE 4-3 Flow chart for calculation of the pumpjet efficiency

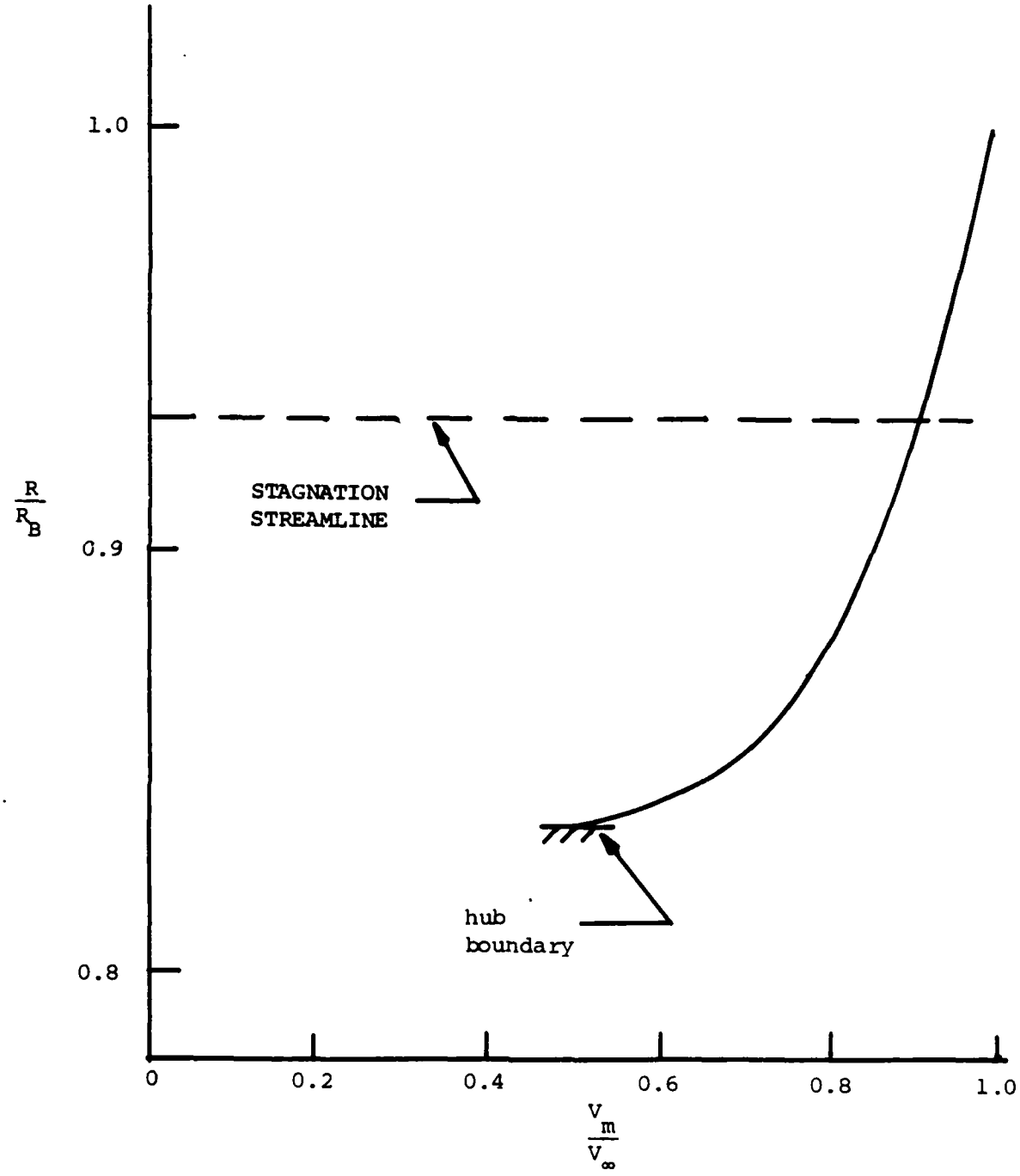

FIGURE 4-4 Meridional velocity at station (1) of Figure 4-2

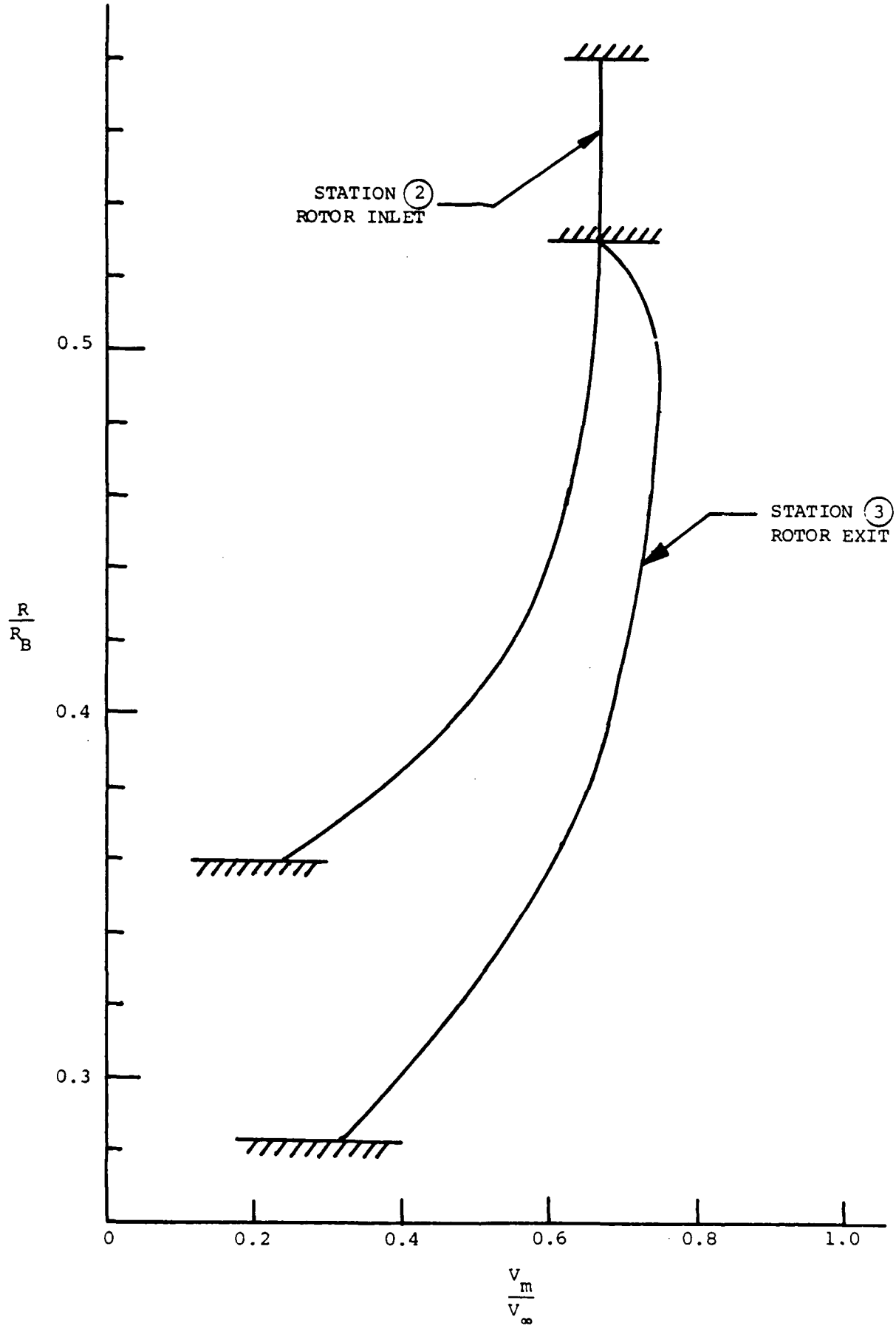

FIGURE 4-5 Meridional velocity distributions at stations (2) and (3) of Figure 4-2

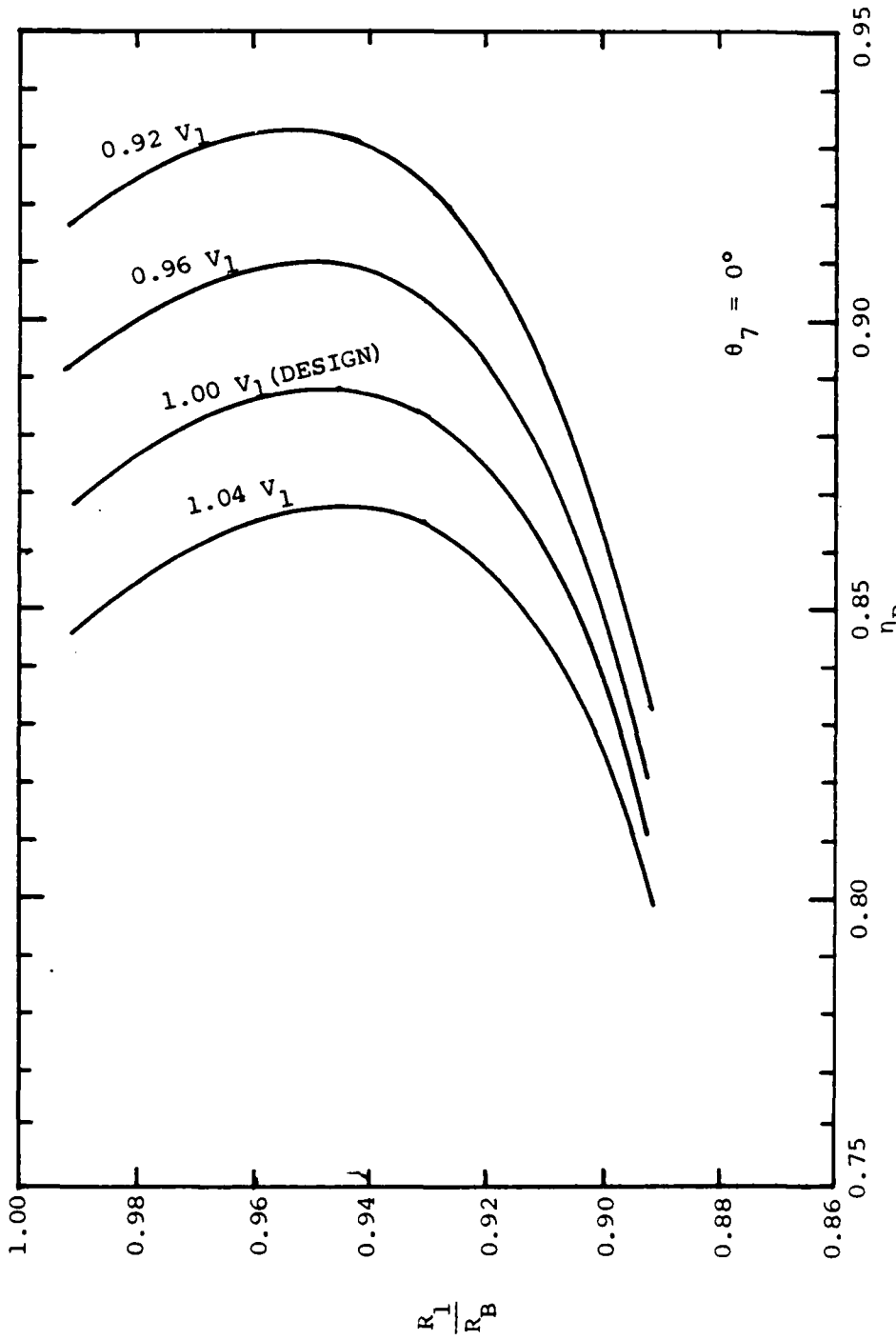

FIGURE 4-6 Calculated propulsive efficiency as functions of R_1/R_B (stagnation streamline radius) with the incoming flow velocity amplification factor, $\theta_7 = 0°$

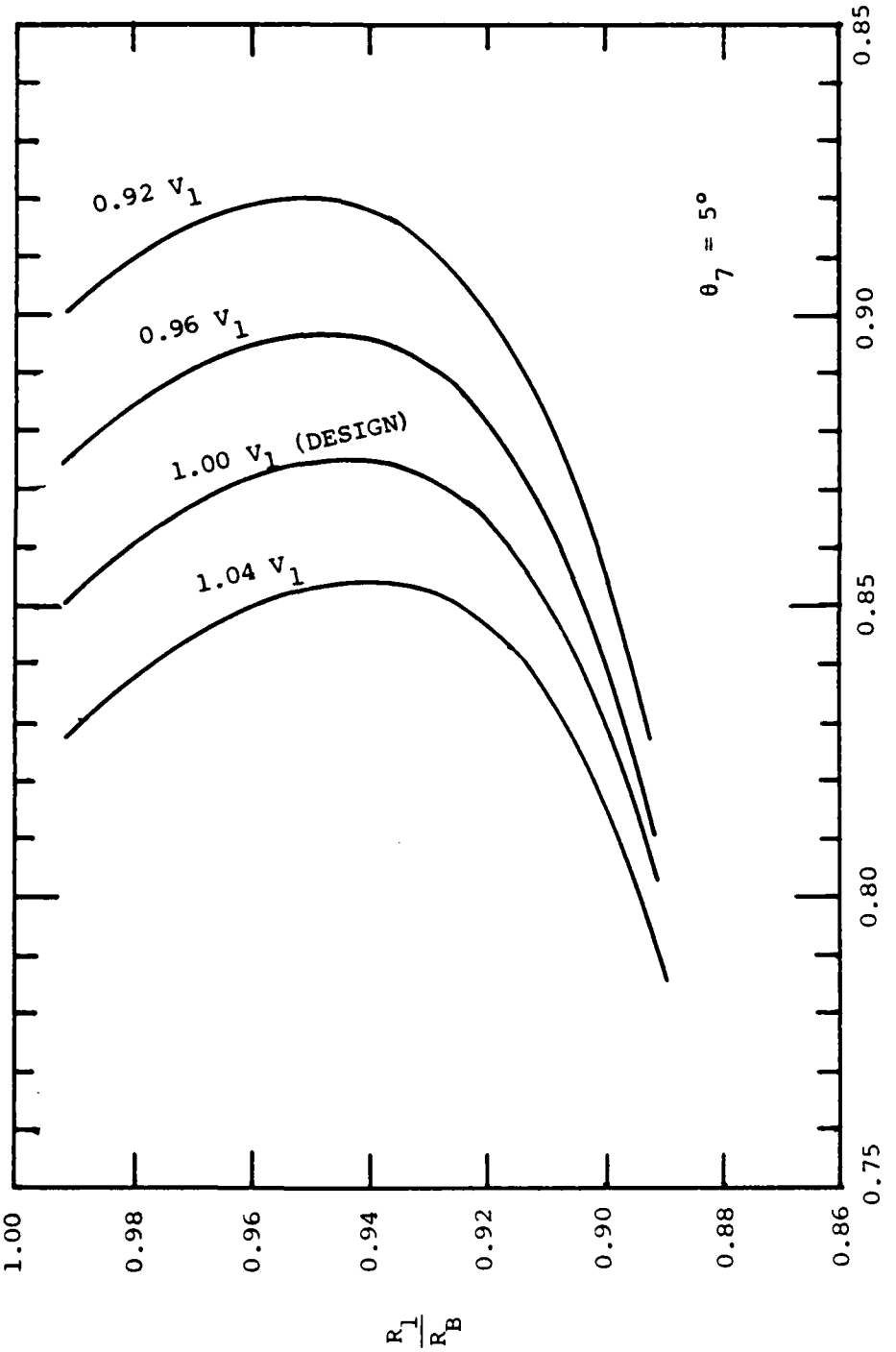

FIGURE 4-7 The same as Figure 4-6, except for $\theta_7 = 5°$

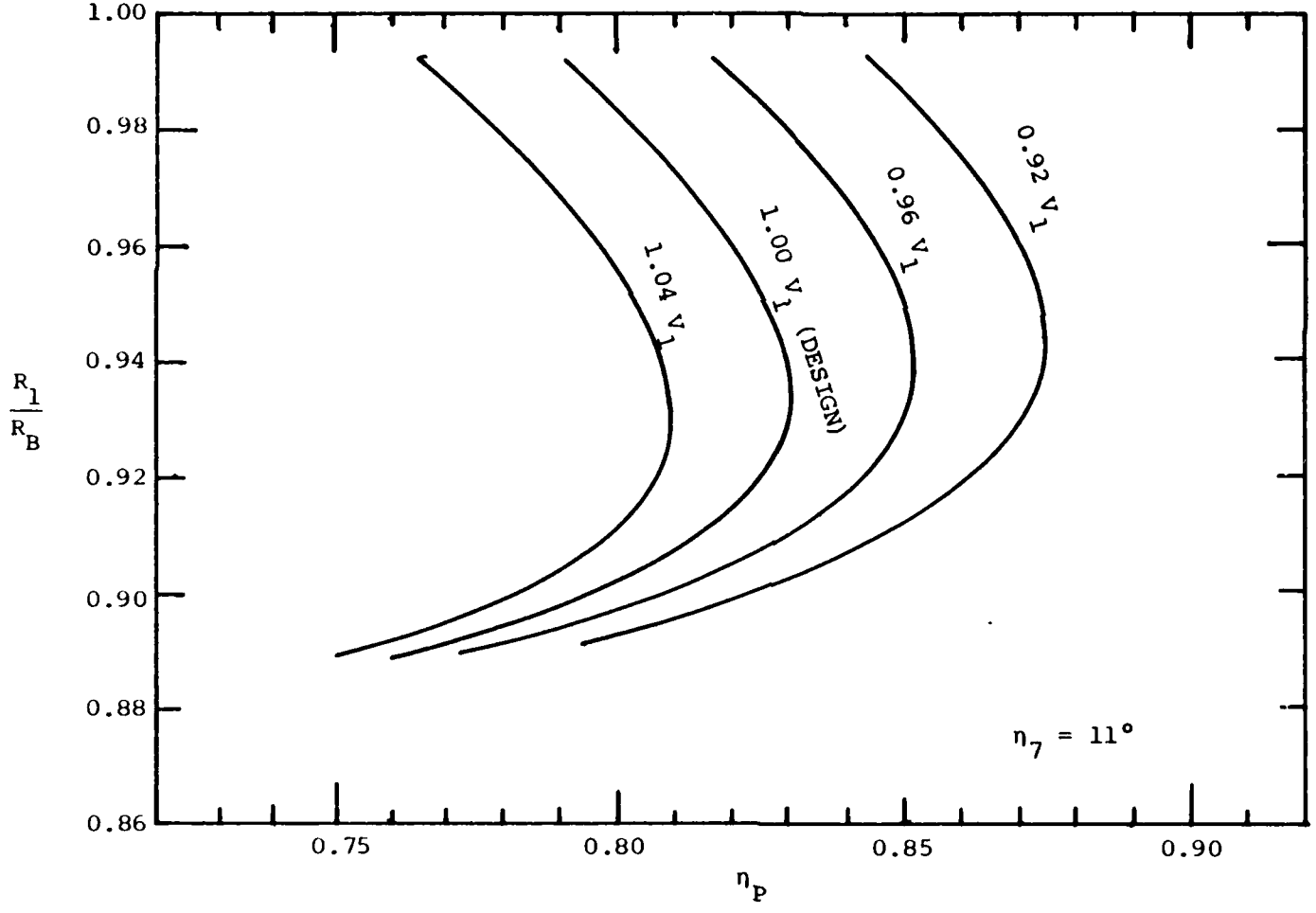

FIGURE 4-8 The same as Figure 4-6, except for θ_7 = 11°

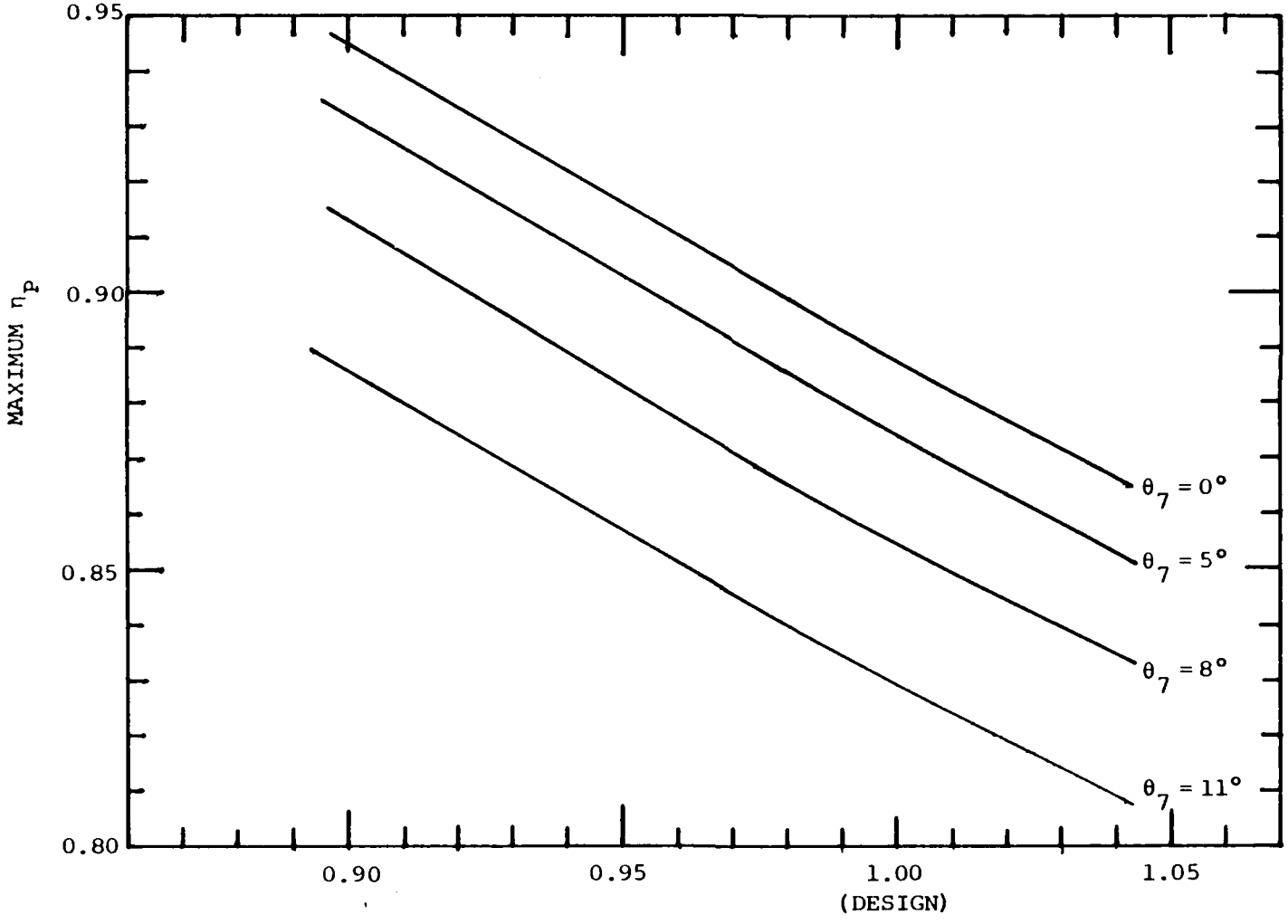

FIGURE 4-9 Maximum propulsive efficiency as a function of the incoming flow velocity amplification factor with θ_7 as a parameter

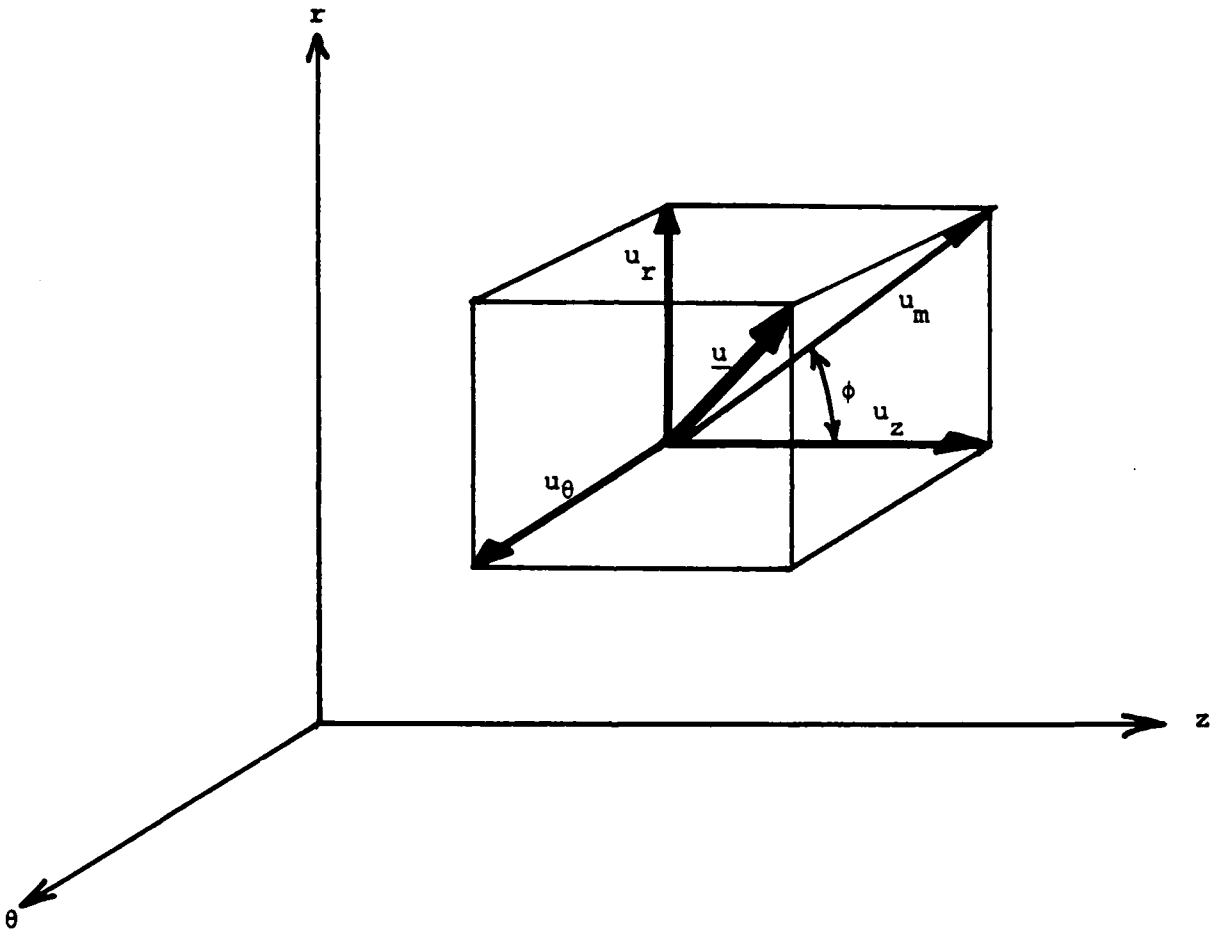

FIGURE 4-10 Velocity diagram

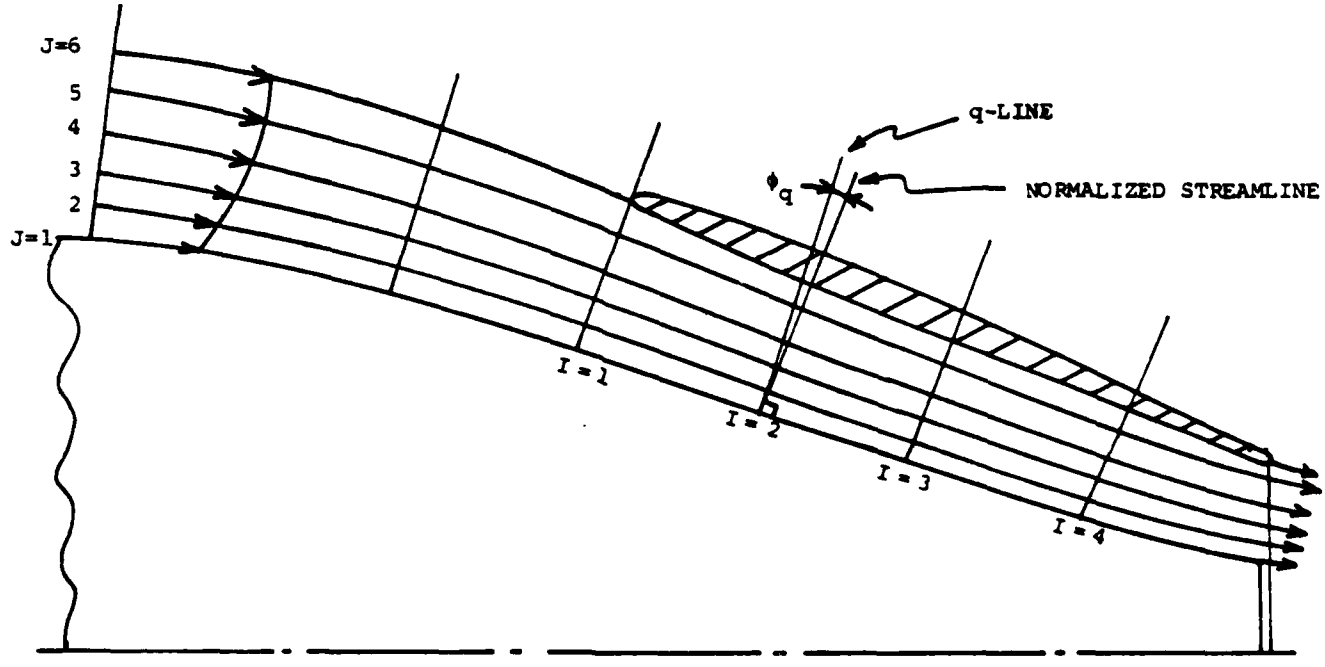

FIGURE 4-11 A schematic flow diagram used for numerical computations on Streamline Curvature Method

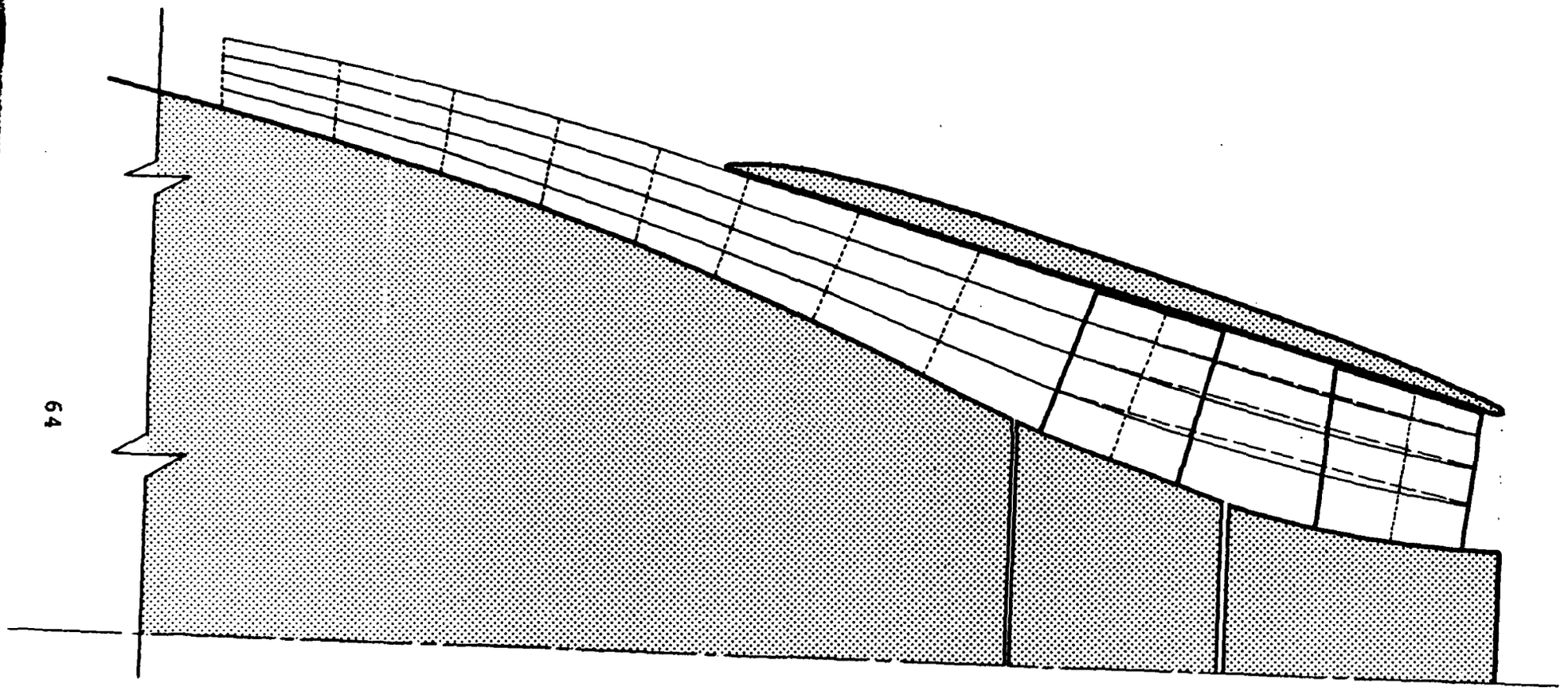

FIGURE 4-12 Calculated results of Streamline Curvature Method for a typical underwater vehicle tail cone with shroud where the solid lines are of the initial guess and dashed lines are the converged solution (the dotted lines are q-lines used for the present computation)

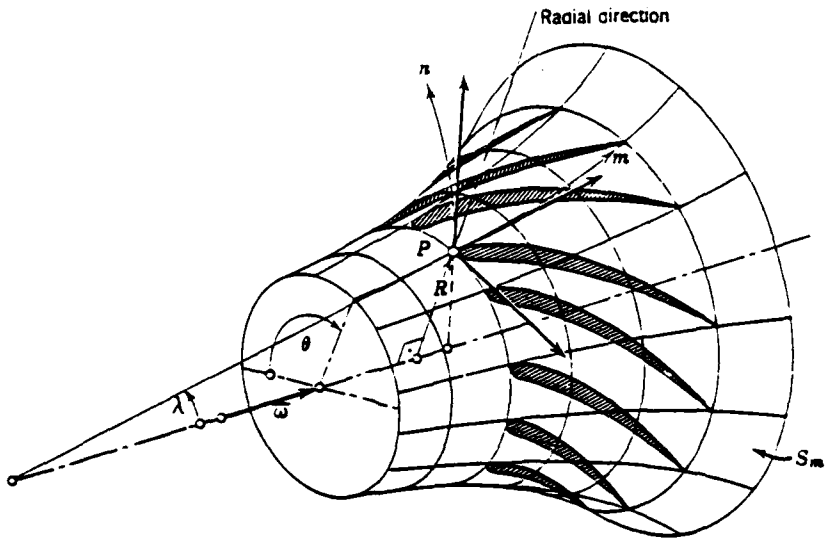

FIGURE 4-13 Axisymmetric stream surface

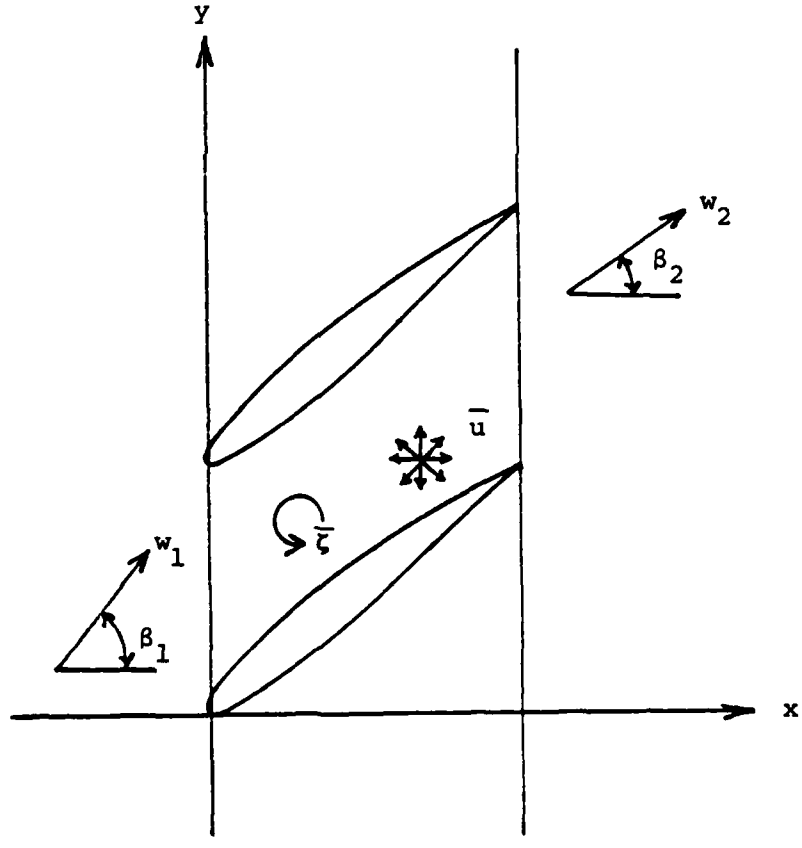

FIGURE 4-14 Flow field on the xy plane

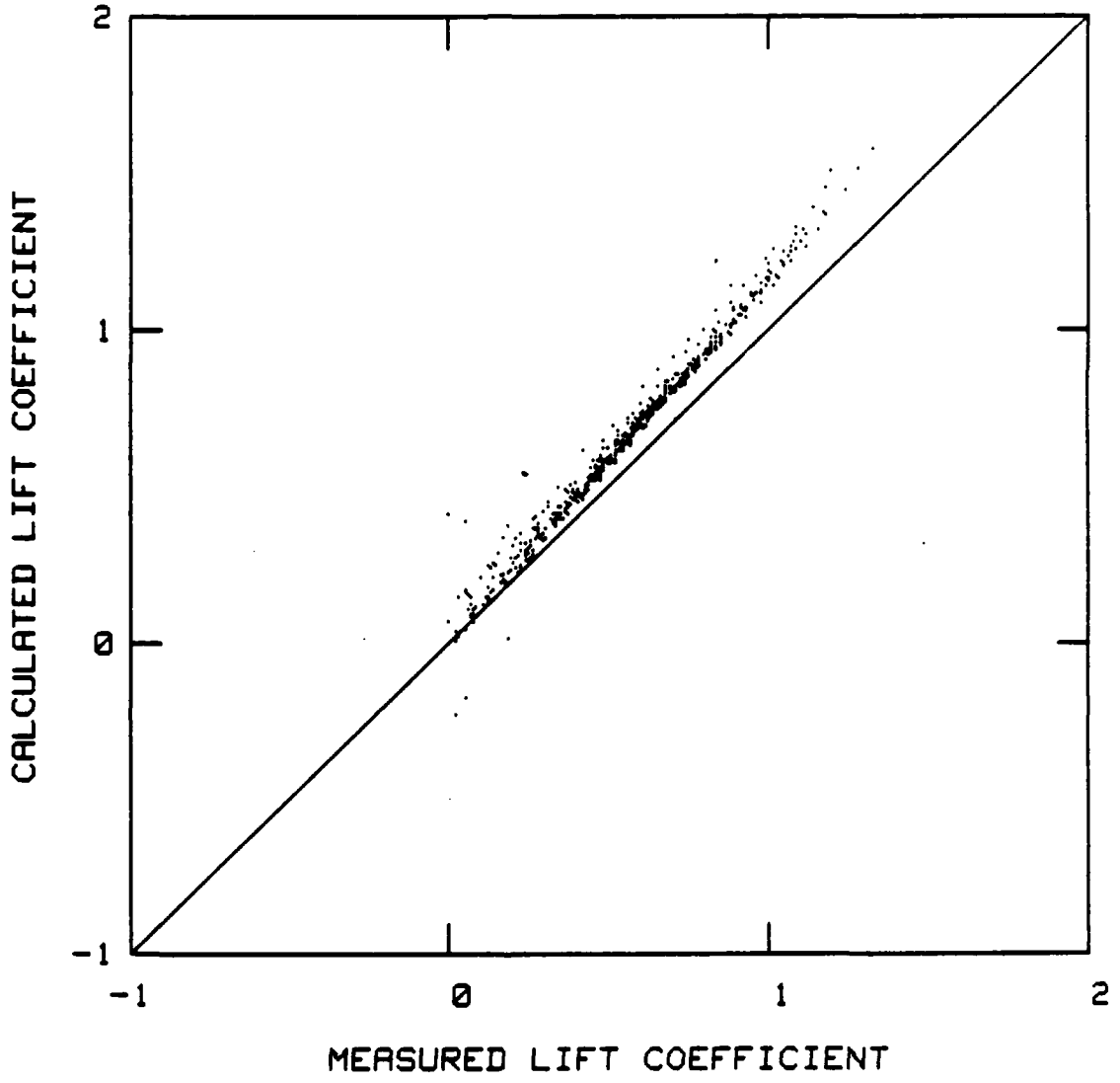

FIGURE 4-15 Comparison of lift coefficient data, without modification factor

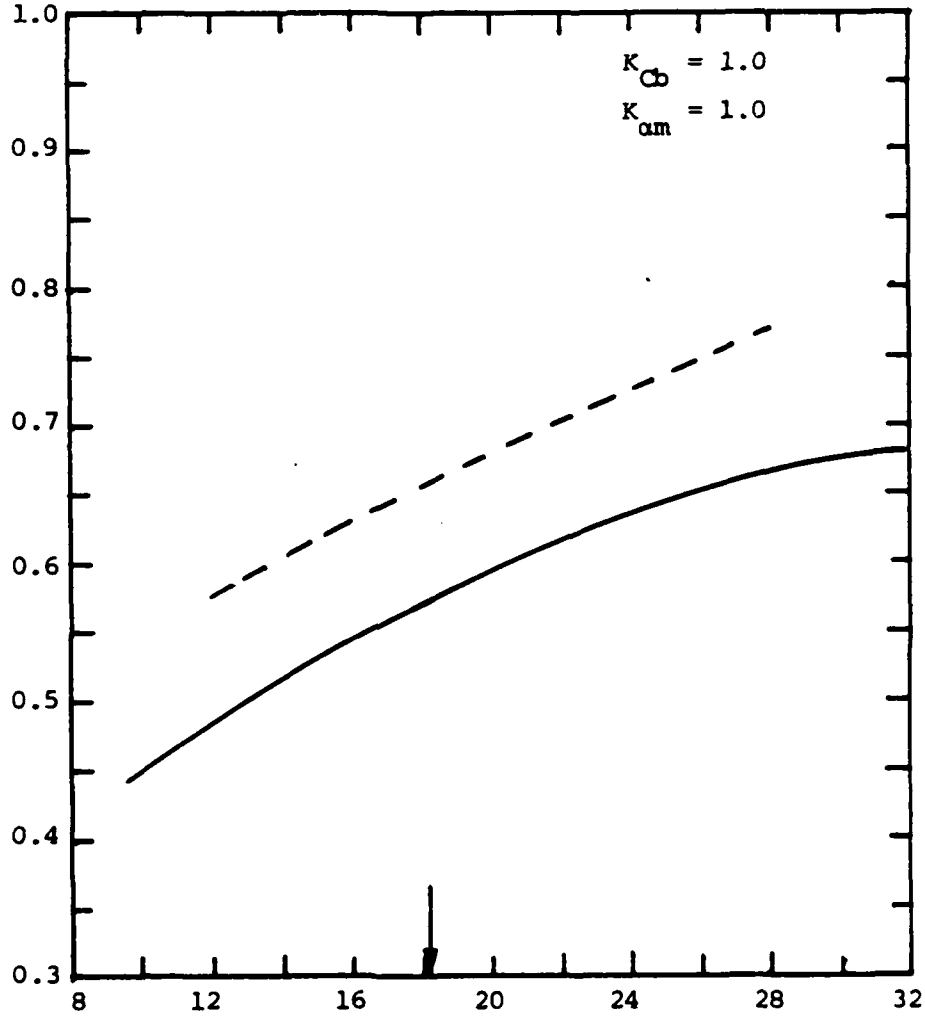

FIGURE 4-16 Comparison of theoretical (dashed line) and measured (solid line) lift coefficient data for NACA 65-(15)10, β_1 = 45°, σ = 1.5 without modification factor. (The arrow indicates the design angle of attack.)

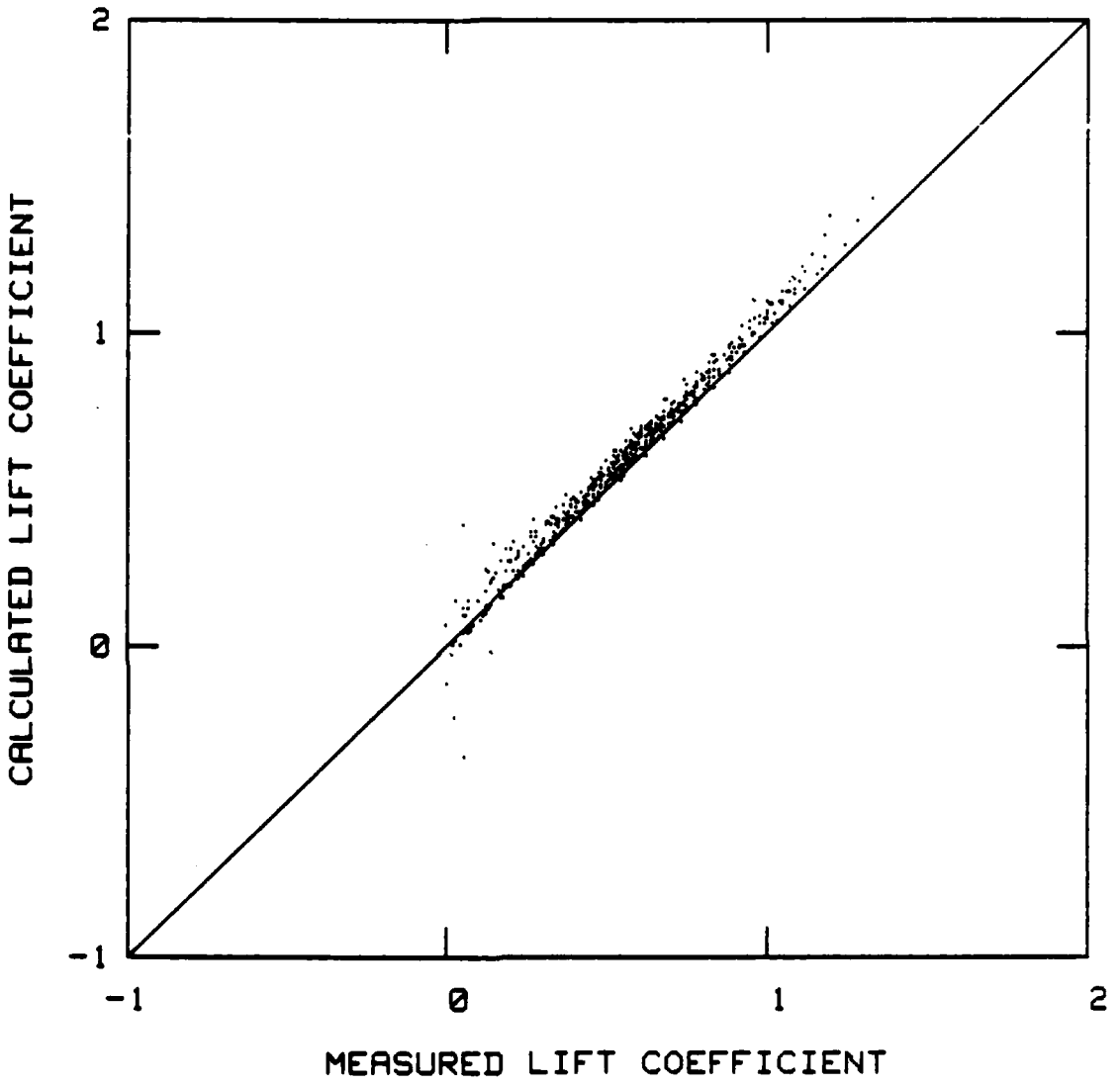

FIGURE 4-17 Comparison of lift coefficient data, with a modification factor of 0.725 applied to C_b

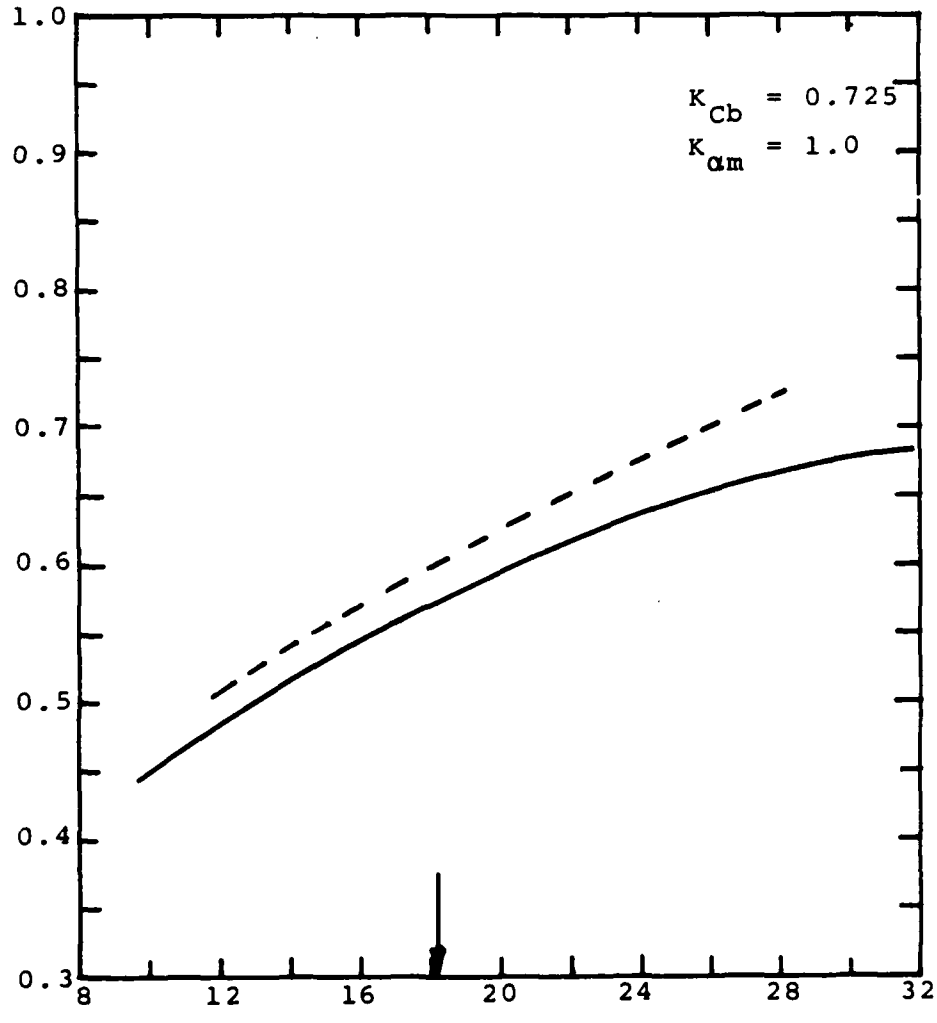

FIGURE 4-18 Comparison of theoretical (dashed line) and measured (solid line) lift coefficient data for NACA 65-(15)10, $\beta_1 = 45°$, $\sigma = 1.5$, with $K_{Cb} = 0.725$ and $K_{\alpha m} = 1$. (The arrow indicates the design angle of attack.)

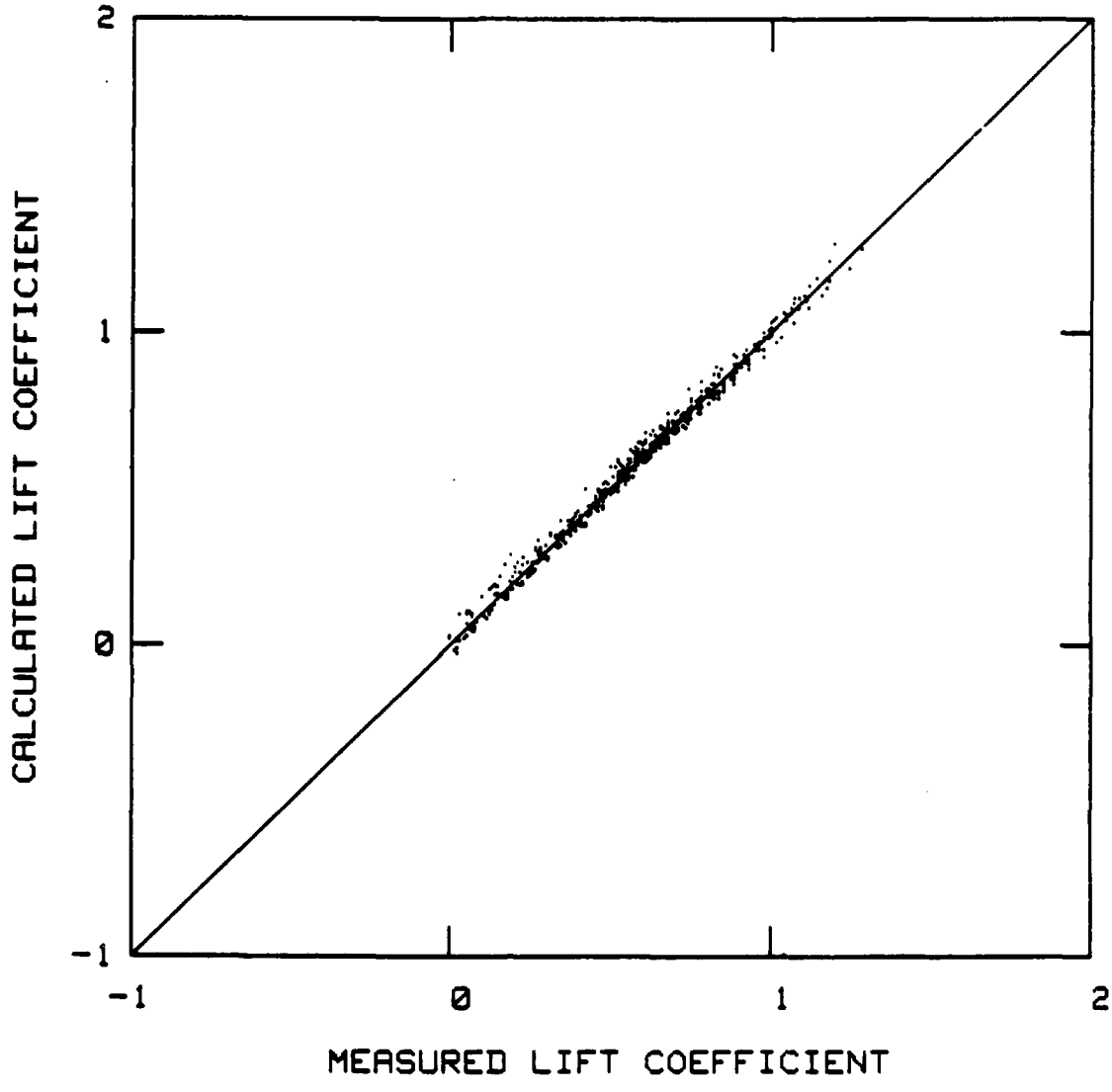

FIGURE 4-19 Comparison of lift coefficient data, with (K_{Cb}, $K_{\alpha m}$) = (0.7, 0.75)

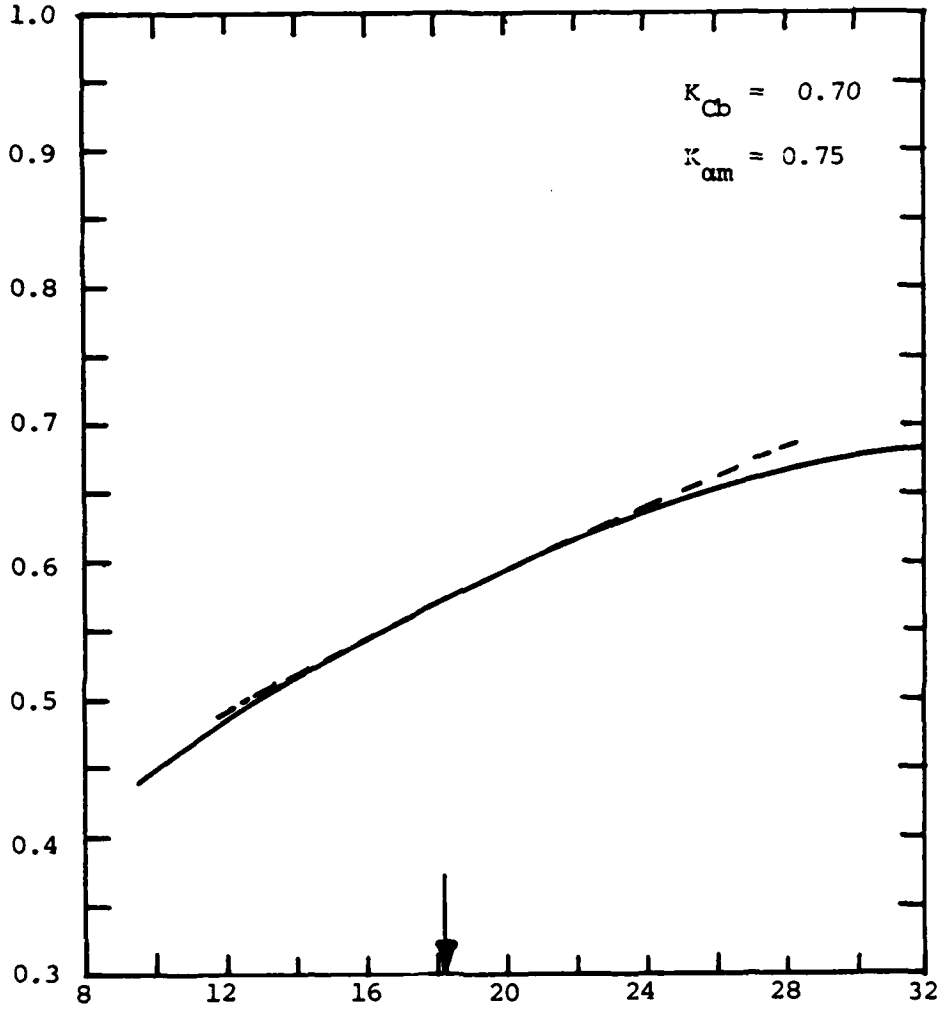

FIGURE 4-20 Comparison of theoretical (dashed line) and measured (solid line) lift coefficient data for NACA 65-(15)10, β_1 = 45°, σ = 1.5, with K_{Cb} = 0.7 and $K_{\alpha m}$ = 0.75. (The arrow indicates the design angle of attack.)

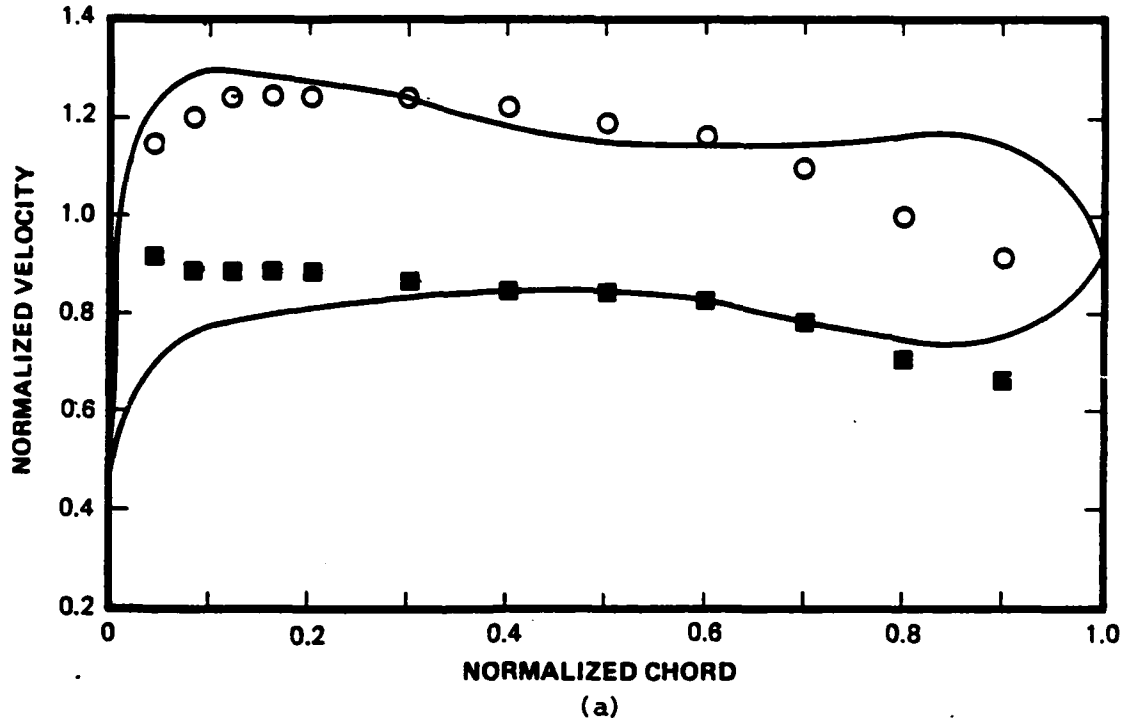

(a)

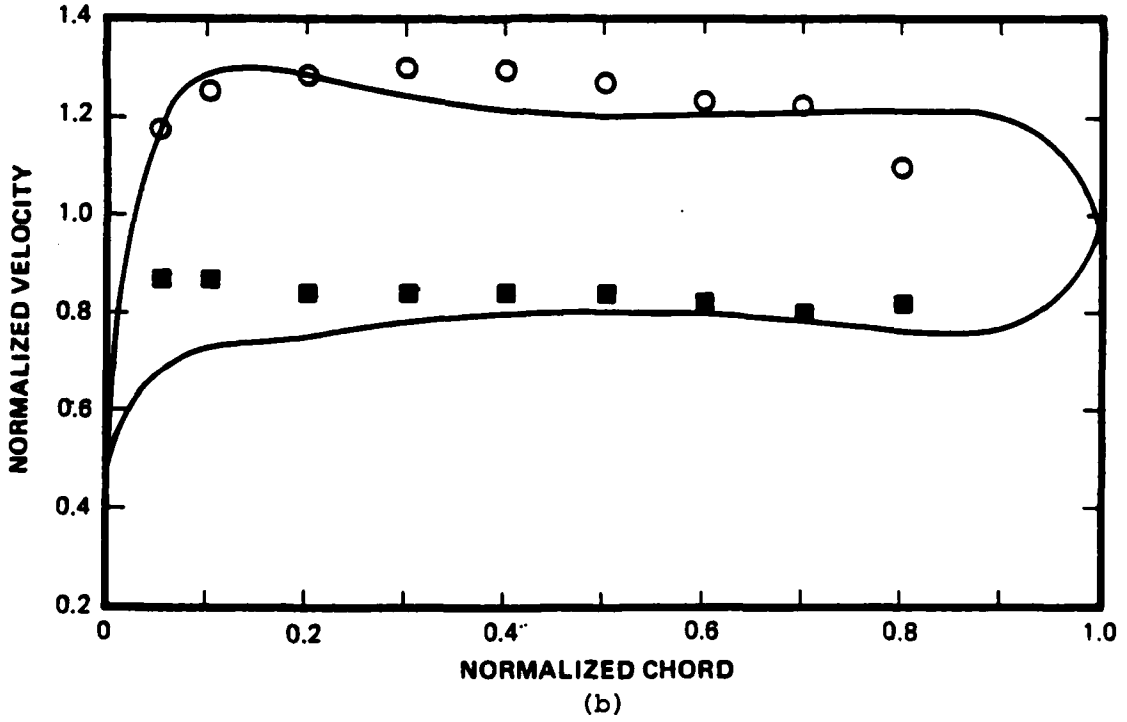

(b)

FIGURE 4-21 Comparison of velocity distribution between the singular perturbation method (——) and test results (O: upper surface, ■: lower surface) of Herrig, et al. (1951) for a) NACA 65-(12)10, β_1 = 45°, solidity = 1.0 and α_1 = 12.1° and b) NACA 65-(12)10, β_1 = 45°, solidity = 0.5 and α_1 = 7.3°

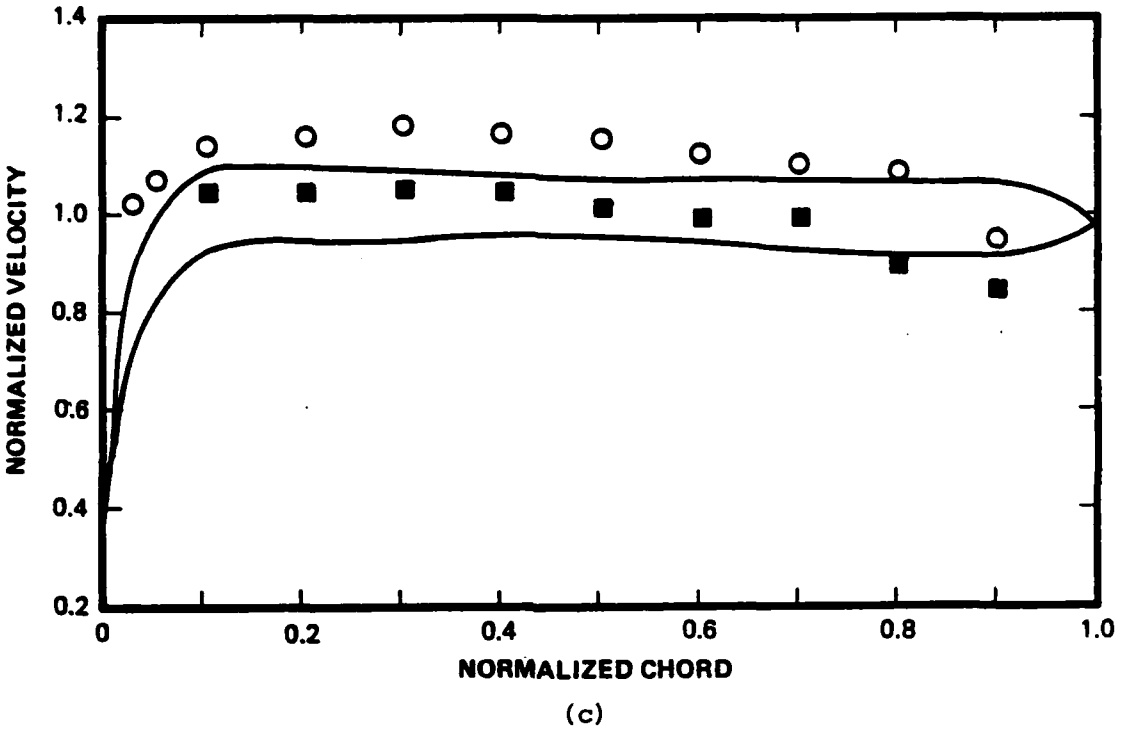

(c)

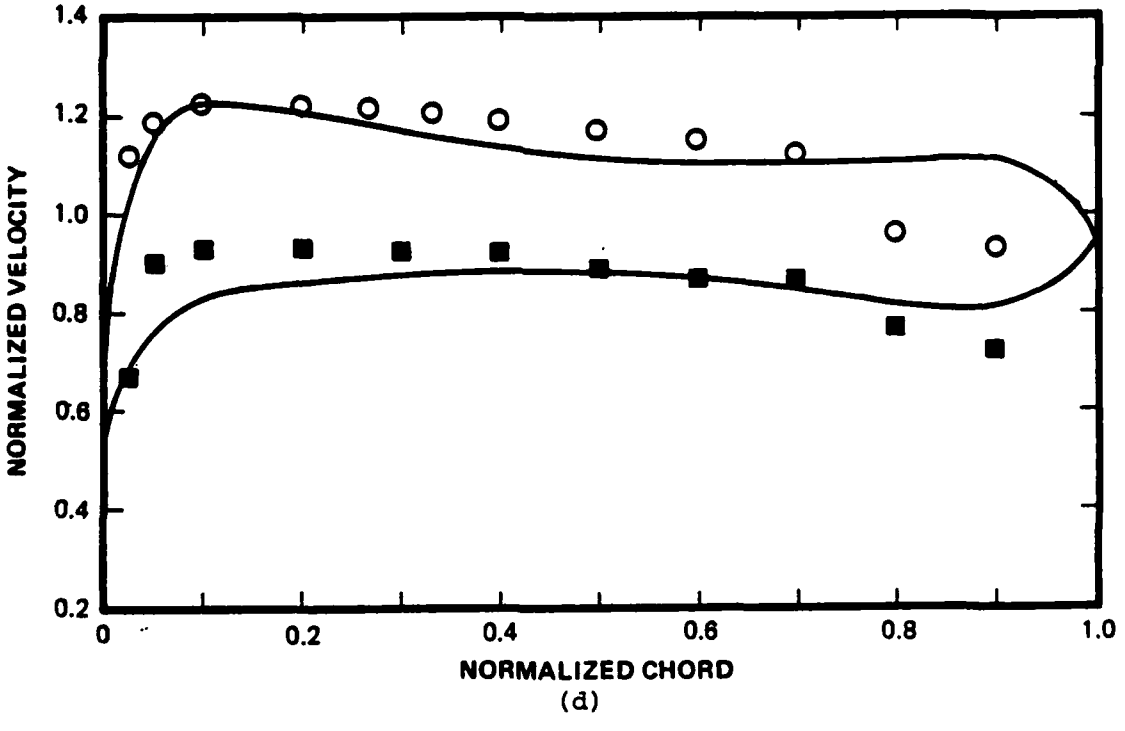

(d)

FIGURE 4-21 (cont'd) c) NACA 65-410, β_1 = 45°, solidity = 1.0 and α_1 = 5°, and d) NACA 65-810, β_1 = 45°, solidity = 1.0 and α_1 = 9.7°

END

8-87

DTIC